



Multi-physics simulation of dendritic growth in magnetic field assisted solidification

Longchao Cao^{a,b}, Dehao Liu^b, Ping Jiang^a, Xinyu Shao^a, Qi Zhou^c, Yan Wang^{b,*}

^aThe State Key Laboratory of Digital Manufacturing Equipment and Technology, School of Mechanical Science and Engineering, Huazhong University of Science & Technology, Wuhan 430074, PR China

^bWoodruff School of Mechanical Engineering, Georgia Institute of Technology, Atlanta, GA 30332, USA

^cSchool of Aerospace Engineering, Huazhong University of Science & Technology, Wuhan 430074, PR China

ARTICLE INFO

Article history:

Received 14 January 2019

Received in revised form 25 August 2019

Accepted 31 August 2019

Keywords:

Thermoelectric current

Magnetic field

Solidification

Lattice Boltzmann method

Phase-field method

ABSTRACT

Magnetic field assisted casting and welding attracted research attentions in the recent decades because it has been observed that the inter-dendritic flow of liquid metals can be controlled by the imposed external magnetic field. However, the underlying mechanism of dendritic growth under a magnetic field is still not fully understood because of the limitations in in-situ experimental methods. To elucidate the mechanism, a new multi-physics model is proposed in this work to simulate the dendritic growth under the influence of an external magnetic field with the consideration of the natural convection. In this model, the physics of solute transport, phase transition via phase field method, natural convection and thermoelectric magnetohydrodynamics via lattice Boltzmann method are tightly coupled. Simulation reveals that intense thermoelectromagnetic convection occurs in the vicinity of the solid-liquid interface, and vortices are generated between dendritic arms. It is shown that the thermoelectromagnetic convection has a major influence on dendritic morphology. The simulation results help explain the experimental observation of curved solidification front and tilted primary trunks. The simulation model is validated by comparing the microstructure morphology and composition distribution with experimental results.

© 2019 Elsevier Ltd. All rights reserved.

1. Introduction

Applying a magnetic field to the casting or welding process has gained research attentions in recent decades. The external magnetic field can affect the melt flow, solute and heat distributions, and dendritic morphology during the solidification process without direct contact of the material. The dendritic morphology has a decisive influence on the mechanical properties of products. To improve process performance and product quality, it is critical to understand the underlying solidification mechanism. Studies have been done to explore the influences of different types of magnetic fields on solidification microstructure [1–3]. For instance, a static axial or transverse magnetic field was used to control the interdendritic liquid flow [4–7]. A high-strength magnetic field was adopted to align the crystal orientation [8,9]. A combination of different magnetic fields was applied to take the advantages of both axial and transverse modes [10].

Although the above experimental studies suggest that magnetic field indeed affects the microstructure evolution, they are

just focused on the magnetic damping effect or magnetization effect without studying the thermoelectromagnetic convection (TEMC). The TEMC is a unique convection during magnetic field assisted solidification [11–17]. This convection is driven by the so-called thermoelectric magnetic force (TEMF), which results from the interaction between the external magnetic field and thermoelectric current at the solid-liquid interface. In the field of metallurgy, Shercliff [18] proposed the first theory of thermoelectromagnetic convection. Since then, the influence of TEMC on dendritic morphology during solidification has been studied experimentally. Moreau et al. [13] studied the thermoelectric effect during solidification by analysis of solidified microstructures and concluded that TEMC led to more developed dendrites and larger freckles. Li et al. [14] observed the effects of magnetic field on both the solidification front shape and crystal morphology at different scales. To investigate the effects of TEMC directly, Wang et al. [19,20] observed the solidification interface through in-situ synchrotron X-ray radiography. The real-time observation indicated that the shape of interface varies with the change of transverse magnetic field density. It was also found that there is a balance between the TEMC and solute-induced convection. It was speculated that the redistribution of

* Corresponding author.

E-mail address: yan.wang@me.gatech.edu (Y. Wang).

the alloy compositions induced by the TEMC was the reason for interface distortions. Nevertheless, the analysis of solidified microstructure cannot reveal the actual dendritic evolution. Furthermore, the in-situ observation of some physical quantities, such as melt flow velocity, melt pool temperature, and composition, is still challenging.

Compared to experimental studies, simulation is more cost-effective to reveal the cause-effect relations. Numerical simulations have been utilized to understand the effect of TEMC. Couvat et al. [21] used the finite element and finite volume methods to simulate the TEMC between grains. However, in their simulations, every grain was simplified as a rigid sphere. Neither heat transfer nor solute transport was considered. Kao [17] extended the enthalpy-based method to investigate the effect of TEMC on the dendritic growth during solidification with a high undercooling. The dendritic growth, TEMC, and the transport of heat and solute were coupled. However, the buoyancy was neglected and the details of the dendrite were unavailable.

To elucidate the physical details of the solid-liquid phase transition during solidification, mesoscale multi-physics simulations are necessary and useful. Particularly, phase field method (PFM) has been widely used in the simulation of solidification processes. In PFM, a continuous variable named phase field is applied to describe the microstructure evolution [22–24]. Not only good accuracy, PFM also provides the convenience of integrating with other physical fields [25–29]. Recently, PFM started being applied to simulate magnetic field assisted solidification. Chang et al. [28] studied the effects of a strong magnetic field on the dendritic growth using PFM. Their simulation results showed that the primary arm and side branches were coarsened under a strong magnetic field. Feng et al. [27] investigated the sensitivities of changing nucleation energy and diffusion activation energy under a magnetic field using PFM. The results demonstrated that an external magnetic field could promote the formation of texture. Both of the above studies focused on the change of free energy under the external magnetic field and crystal evolution, whereas the effects of TEMC on dendritic growth were not considered.

Here, a multi-physics simulation approach is taken with the simultaneous considerations of TEMC, solute transport, and buoyancy in phase transition. This is an extension of our recently developed phase field and thermal lattice Boltzmann method (PF-TLBM) [22,30] where heat transfer, latent heat, and melt flow are integrated with the simulation of dendritic growth. For fluid flows with complex boundaries, lattice Boltzmann method (LBM) [22,31–33] has computational advantages compared to conventional methods such as finite volume and finite element. In this paper, the new integrated model called phase field-magnetic field-lattice Boltzmann method (PF-MF-LBM) is proposed to simulate the magnetic field assisted solidification process with natural convection. In PF-MF-LBM, the solute transport, phase transition, natural convection, and TEMC are coupled concurrently to predict the solute distribution and dendritic morphology.

The remaining of the paper are organized as follows. In Section 2, the formulation of TEMF, PFM, and LBM are introduced. In Section 3, two simulation cases are used to demonstrate the proposed PF-MF-LBM model. In the first case in Section 3.1, the effect of the external magnetic field is illustrated with the solidification of Al-Cu alloy in casting. The simulation result is qualitatively compared with experimental observations reported in the literature. In the second case in Section 3.2, the magnetic field assisted laser welding is simulated, and the predicted composition distributions from simulation are quantitatively compared with our experimental measurements. In Section 4, the conclusion and a brief outlook are given.

2. Methodology

In this section, the thermoelectric magnetic effect during solidification is first introduced. Then the proposed PF-MF-LBM model is presented.

2.1. Thermoelectric effects and TEMF model

2.1.1. The Seebeck effect

The thermoelectric effects at the solid-liquid interface during solidification have been observed in physical experiments [11,19,34]. Three main thermoelectric effects are distinguished, including Peltier, Thomson, and Seebeck effects [18]. This study is focused on the Seebeck effect because Peltier and Thomson effects are much weaker [35,36].

The diffusion speed of charge carriers in materials is a function of temperature. There is a concentration gradient of charge carriers along the thermal gradient when the thermal gradient is imposed. The revised Ohm's law by incorporating the Seebeck effect is given as

$$\frac{\mathbf{J}}{\kappa} = \mathbf{E} - S\nabla T + \mathbf{u}_l \times \mathbf{B} \quad (1)$$

where \mathbf{J} denotes the current density, κ is the electric conductivity, \mathbf{E} is the electric field, S is Seebeck coefficient, T is the temperature field, ∇T is the thermal gradient, \mathbf{u}_l is the velocity of the liquid, and \mathbf{B} is the imposed magnetic field. The second term $S\nabla T$ in the right-hand side of Eq. (1) represents the internal electric field formed in the materials caused by the Seebeck effect [18]. The third term $\mathbf{u}_l \times \mathbf{B}$ captures the electromotive force, which is caused by a conductor traveling across the magnetic field. Seebeck coefficient is related to the material phase and local temperature. However, the Seebeck coefficient of the same phase does not change much in the temperature range of solidification [37]. For simplification, the Seebeck coefficient is assumed to be a constant value for each phase.

When a thermal gradient is imposed to a stationary material with a constant Seebeck coefficient and neither external electric nor magnetic field is applied, the electromotive force will be generated. However, no current will be generated within the materials, as shown by

$$\nabla \times \frac{\mathbf{J}}{\kappa} = \nabla \times (-S\nabla T) = -\nabla S \times \nabla T - S\nabla \times \nabla T = 0 \quad (2)$$

which means that the thermoelectric field $-S\nabla T$ is irrotational. Even when the Seebeck coefficient S is a function of temperature T , the term $\nabla S \times \nabla T$ still vanishes. Therefore, two requirements or conditions must be satisfied before the thermoelectric current is generated. First, there is a thermal gradient at the interface region of different materials or phases. Second, the thermal gradient should not be parallel to the gradient of the Seebeck coefficient. That is, the curl of the thermoelectric field is not equal to zero. During the solidification process, typically there is a thermal gradient along the solid-liquid interface, and the solid and liquid phases always have different Seebeck coefficient values. Therefore, both requirements for generating thermoelectric current are met.

Fig. 1 illustrates the thermoelectric current at the solid-liquid interface. Thermoelectric current is generated when the thermal gradient ∇T exists along the vertical direction. The difference of thermoelectric potential between point A and point B.

$$V_{AB} = \oint \frac{\mathbf{J}}{\kappa} \cdot d\mathbf{r} \quad (3)$$

drives the current in the circuit A-B-A, where the integral is along the path from point A to point B. If no external electric or magnetic

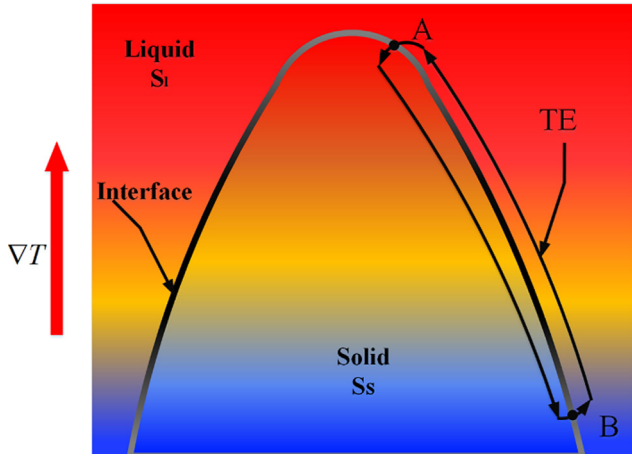


Fig. 1. The schematic illustration of the thermoelectric (TE) current generated at the solid-liquid interface with a thermal gradient ∇T .

field is applied, V_{AB} can be calculated by integrating the thermoelectric field along the circuit path in the current flow direction as

$$\begin{aligned} V_{AB} &= \oint (-S\nabla T) \cdot d\mathbf{r} \\ &= \int_A^B S_l \nabla T \cdot d\mathbf{r} - \int_A^B S_s \nabla T \cdot d\mathbf{r} \\ &= \int_{T_A}^{T_B} (S_l - S_s) dT \\ &= \Delta S \Delta T \end{aligned} \quad (4)$$

where S_s is the Seebeck coefficient of the solid phase, and S_l is the Seebeck coefficient of the liquid phase, T_A and T_B are the temperatures at locations A and B, respectively.

2.1.2. The thermoelectric magnetic force

As mentioned in Section 2.1.1, because of the thermoelectric potential difference at the solid-liquid interface, an electric current flow is generated across the interface to form a closed-loop circulation. The conservation of current is given by

$$\nabla \cdot \mathbf{J} = 0 \quad (5)$$

By substituting Eq. (1) into Eq. (5), we receive

$$\nabla \cdot \mathbf{E} - \nabla \cdot (S\nabla T) + \nabla \cdot (\mathbf{u}_l \times \mathbf{B}) = 0 \quad (6)$$

The solid-liquid interface has a finite thickness instead of a sharp interface. The solidification domain thus is split into three independent subdomains (solid grain region, interface region, and bulk liquid region) to obtain the potential distribution.

In the liquid region, the Seebeck coefficient is assumed to be constant, and there is no thermoelectric current. Therefore, the second term $\nabla \cdot (S\nabla T)$ in the left-hand side of Eq. (6) vanishes. By substituting $\mathbf{E} = -\nabla V$ into Eq. (6), we have the Poisson equation

$$\nabla^2 V = \nabla \cdot (\mathbf{u}_l \times \mathbf{B}) \quad (7)$$

where V is the electric potential. In the solid dendrite region, dendrite moves much slower than bulk liquid. Therefore, the motion of the dendrite can be neglected. The Poisson equation within the grain becomes

$$\nabla^2 V = 0 \quad (8)$$

In the interface region,

$$V_{int} = \Delta S \Delta T \quad (9)$$

is the electric potential. Within the interphase region, the composition varies continuously. The Seebeck coefficient within the interface region [38,39] is

$$S = S_l \phi_l + S_s \phi \quad (10)$$

where ϕ represents the local solid phase fraction and $\phi_l = 1 - \phi$ is the local liquid phase fraction. After the potential is obtained, the current density is calculated as

$$\mathbf{J} = -\kappa \nabla V \quad (11)$$

where the overall electric conductivity κ is similarly estimated from those in liquid κ_l and solid κ_s , given by

$$\kappa = \phi_l \kappa_l + \phi \kappa_s \quad (12)$$

When an external magnetic field is imposed during solidification, a Lorentz force caused by the mutual interaction between the magnetic field and thermoelectric current triggers a forced flow within the interdendritic network, which is the so-called TEMC. The Lorentz force [40]

$$\mathbf{F}_{TEMF} = \mathbf{J} \times \mathbf{B} \quad (13)$$

is the cross product of the thermoelectric current and magnetic flux density, which is perpendicular to both the magnetic field and thermoelectric current. The Lorentz force in the interface region is larger than the ones in other regions. It gradually vanishes towards the locations far away from the interface because the thermoelectric current is concentrated in the vicinity of the solid-liquid interface. The fluid flow is driven by the Lorentz force, which determines the velocity field distribution. The Lorentz force can be incorporated into the classic Navier-Stokes equation of liquid flow as a force source term. As a result, the thermoelectric effect is coupled in the bulk fluid flow.

2.2. Phase field model

In this section, the formulation of PFM is introduced. As an extension of our previous work [22], the noise is introduced to consider the instability of dendritic growth, which is also different from most of phase field formulations (e.g. [23,26,41]).

The generalized free energy functional

$$F = \int_{\Omega} (f^{GB} + f^{CH}) d\Omega \quad (14)$$

is the sum of the interfacial free energy f^{GB} and chemical free energy f^{CH} in domain Ω . The interfacial free energy is given by

$$f^{GB} = \frac{4\sigma^*(\mathbf{n})}{\eta} \left\{ |\nabla \phi|^2 + \frac{\pi^2}{\eta^2} \phi(1-\phi) \right\}, \quad (15)$$

where $\sigma^*(\mathbf{n})$ is the anisotropic interfacial energy stiffness, η is the width of the thin interface between solid and liquid phases, $\mathbf{n} = \nabla \phi / |\nabla \phi|$ is the local normal vector of the interface, ϕ is the phase field which denotes the local fraction of solid phase. The anisotropic interfacial energy stiffness is defined as

$$\sigma^* = \sigma + \frac{\partial^2 \sigma}{\partial \theta^2} = \sigma_0^* [1 - 3\varepsilon^* + 4\varepsilon^* (n_x^4 + n_y^4)] \quad (16)$$

where σ is the interfacial energy, $\theta = \arctan(n_y/n_x)$ is the local angle between the normal direction \mathbf{n} and the principal x direction on the interface, σ_0^* is the prefactor of interfacial energy stiffness and ε^* is the anisotropy strength of interfacial energy stiffness.

The chemical free energy is defined as

$$f^{CH} = h(\phi) f_s(C_s) + h(1-\phi) f_l(C_l) + \mu(C - (\phi C_s + \phi_l C_l)) \quad (17)$$

where C_s and C_l are the solute composition in solid and liquid phases respectively, C is the overall composition of the solute, $f_s(C_s)$ and $f_l(C_l)$ are the chemical bulk free energy densities of the solid and liquid phases respectively, μ is the generalized chemical potential of solute introduced as a Lagrange multiplier to ensure the solute mass conservation between the phases, and

$$h(\phi) = \frac{1}{4} \left[(2\phi - 1) \sqrt{\phi(1-\phi)} + \frac{1}{2} \arcsin(2\phi - 1) \right] \quad (18)$$

is the weight function.

The kinetic equations for the phase field and composition field are

$$\dot{\phi} = M_{eff} \left\{ \sigma^*(\mathbf{n}) \left[\nabla^2 \phi + \frac{\pi^2}{\eta^2} \left(\phi - \frac{1}{2} \right) \right] + \frac{\pi}{\eta} \sqrt{\phi(1-\phi)} (1 + \hat{\theta}(\mathbf{r}, t)) \Delta G \right\} \quad (19)$$

and

$$\dot{C} + \mathbf{u}_l \cdot \nabla [(1-\phi)C_l] = \nabla \cdot [D_l(1-\phi)\nabla C_l] + \nabla \cdot \mathbf{j}_{at} \quad (20)$$

respectively, where D_l is the diffusion coefficient of liquid, and \mathbf{u}_l is the velocity of the liquid. The effective interface mobility is given by

$$M_{eff} = \frac{8D_l}{\Delta S_{fus} \eta m_l (C_l - C_s)} \quad (21)$$

where ΔS_{fus} is the entropy difference between the solid and liquid phase [26,30], and m_l is the slope of liquidus. $\hat{\theta}(\mathbf{r}, t)$ is the white noise with the variance

$$\langle \hat{\theta}(\mathbf{r}, t), \hat{\theta}(\mathbf{r}', t') \rangle = A \delta(\mathbf{r} - \mathbf{r}') \delta(t - t') \quad (22)$$

where A is the amplitude of the fluctuations, δ is the Dirac delta function, \mathbf{r} is the space vector, and t is the time. This noise term causes fluctuations at the solid-liquid interface, which captures the natural instability of a dendritic structure [42–44]. The anti-trapping current is given by

$$\mathbf{j}_{at} = \frac{\eta}{\pi} \sqrt{\phi(1-\phi)} (C_l - C_s) \dot{\phi} \frac{\nabla \phi}{|\nabla \phi|} \quad (23)$$

which is used to remove the effect of numerical solute trapping caused by the diffusion of the interface. $\Delta G = \Delta S_{fus}(T_m - T + m_l C_l)$ is the driving force between the liquid and solid phases, where T_m is the melting temperature of a pure substance. To calculate the composition of liquid and solid phases during solidification, a linear phase diagram is utilized with the constant partition coefficient $k = C_s/C_l$ [45].

2.3. Lattice Boltzmann method

To simplify the model, the densities of the liquid and solid phases are assumed to be equal and constant. The solid phase is assumed to be stationary. To obtain the velocity field of liquid phase caused by the thermoelectric magnetic force and the buoyancy force, the conservation equations of mass and momentum are fully coupled [46–48], given by

$$\nabla \cdot (\phi_l \mathbf{u}_l) = 0 \quad (24)$$

and

$$\frac{\partial}{\partial t} (\phi_l \mathbf{u}_l) + \nabla \cdot (\phi_l \mathbf{u}_l \mathbf{u}_l) = -\frac{\phi_l}{\rho} \nabla P + \nabla \cdot [v \nabla (\phi_l \mathbf{u}_l)] + \mathbf{F}_d + \mathbf{F}_{TEMF} + \mathbf{F}_{bu} \quad (25)$$

respectively, where ρ is the liquid density, P is the pressure, v is the kinematic viscosity, \mathbf{F}_{TEMF} is the Lorentz force source term in Eq. (13), and

$$\mathbf{F}_d = -h^* \phi_l \rho v \frac{\phi^2}{\eta^2} \mathbf{u}_l \quad (26)$$

is the dissipative force caused by the friction between solid and liquid, where $h^* = 147$ is the numerical coefficient fitted from the calculation of Poiseuille flow in a channel with diffuse walls [49]. The buoyancy force is given by

$$\mathbf{F}_{bu} = -\frac{1}{\rho} \frac{\partial \rho}{\partial C} \mathbf{g} (C_l - C_0) (1 - \phi) - \frac{1}{\rho} \beta_T \mathbf{g} (T - T_0) (1 - \phi) \quad (27)$$

where \mathbf{g} is the gravitational acceleration [46], β_T is the thermal expansion coefficient, C_0 is the initial composition of the liquid phase and T_0 is the reference temperature [50]. The first term in the right-hand side of Eq. (27) represents the solutal buoyancy force, whereas the second term in the right-hand side of Eq. (27) is the thermal buoyancy force.

In this work, the LBM is adopted to solve the conservation equations of mass and momentum because of its advantage in solving fluid flow problems with complex boundary conditions [30,51]. The kinetic equation for the LBM is

$$f_k(\mathbf{x} + \mathbf{c}_k \Delta t, t + \Delta t) = f_k(\mathbf{x}, t) + \frac{f_k^{eq}(\mathbf{x}, t) - f_k(\mathbf{x}, t)}{\tau} + F_k(\mathbf{x}, t) \Delta t \quad (28)$$

where \mathbf{x} is the position vector in a regular spatial lattice, t is the time, $f_k(\mathbf{x}, t)$ is the particle distribution function representing the density, and the index k corresponds to a unique direction in the lattice. The two-dimensional D2Q9 model is used, where each node has eight neighbors. That is, $k = 0$ indicates the node itself, $k = 1$ to 4 are the right, top, left, and down directions, whereas $k = 5$ to 8 are the top-right, top-left, down-left, and down-right directions, respectively. In addition, \mathbf{c}_k is the particle velocity in the k^{th} direction, with magnitude $c = |\mathbf{c}_k| = \Delta x / \Delta t$, where Δx is the grid spacing and Δt is the time step. The dimensionless relaxation time τ is given by

$$\tau = \frac{v}{c_s^2 \Delta t} + 0.5 \quad (29)$$

with the speed of sound $c_s^2 = c^2/3$. Furthermore,

$$f_k^{eq} = \rho \omega_k \left[1 + \frac{\mathbf{c}_k \cdot \mathbf{u}_l}{c_s^2} + \frac{(\mathbf{c}_k \cdot \mathbf{u}_l)^2}{2c_s^4} - \frac{\mathbf{u}_l^2}{2c_s^2} \right] \quad (30)$$

is the equilibrium particle distribution function, and

$$\omega_k = \begin{cases} 4/9, & k = 0 \\ 1/9, & k = 1, \dots, 4 \\ 1/36, & k = 5, \dots, 8 \end{cases} \quad (31)$$

are the weight coefficients in the two-dimensional D2Q9 model. The discrete external force F_k based on the forcing scheme of Guo et al. [52] is given by

$$F_k = \left(1 - \frac{1}{2\tau} \right) \omega_k \left(\frac{\mathbf{c}_k - \mathbf{u}_l}{c_s^2} + \frac{\mathbf{c}_k \cdot \mathbf{u}_l}{c_s^4} \mathbf{c}_k \right) \cdot \mathbf{F}, \quad (32)$$

where $\mathbf{F} = \mathbf{F}_d + \mathbf{F}_{TEMF} + \mathbf{F}_{bu}$ includes the dissipative, Lorentz, and buoyancy forces respectively [30].

The macroscopic quantities of density and velocity of liquid are calculated from f_k 's as

$$\rho = \sum_k f_k \quad (33)$$

and

$$\rho \mathbf{u}_l = \sum_k \mathbf{c}_k f_k + \frac{\Delta t}{2} \mathbf{F} \quad (34)$$

respectively.

2.4. The simulation algorithm in PF-MF-LBM

Multiple physical phenomena are involved in the solidification process with natural convection and TEMC. In the PF-MF-LBM model, different variables are coupled with each other. The major ones include phase field ϕ and its time derivative $\dot{\phi}$, composition

C, thermoelectric current \mathbf{J} , and fluid velocity \mathbf{u}_l . The overall algorithm of PF-MF-LBM is shown in Fig. 2, which includes the following major steps:

1. Set up the computational conditions and initialize the variables.
2. Solve Eqs. (19) and (20) to obtain variables ϕ and C.
3. Compute electric potential V and current \mathbf{J} by solving Eqs. (7), (8), (10) and (11).

4. Compute fluid velocity \mathbf{u}_l from Eq. (34) with the updated force source term \mathbf{F} .
5. Solve the advection equation Eq. (20) to update variable C.
6. Update the boundary conditions.
7. Repeat steps 2–6 until the end of the simulation.

The algorithm is implemented in C++ programming language and integrated with OpenPhase.

3. Simulation results

Here, we use two simulation cases to demonstrate the proposed PF-MF-LBM model. In the first case in Section 3.1, the effect of the external magnetic field is illustrated with the solidification of Al-Cu alloy in casting. The simulation reveals the tendency of asymmetric dendritic growth because of melt flows driven by the thermoelectric magnetic force. The simulation result is qualitatively compared with experimental observations reported in the literature. In the second case in Section 3.2, the magnetic field assisted laser welding is simulated, and the predicted composition distributions from simulation are quantitatively compared with our experimental measurements.

3.1. Magnetic field effect on solidification of Al-Cu alloy

The unidirectional dendritic growth in magnetic field assisted solidification is simulated to demonstrate the proposed PF-MF-LBM model. In a two-dimensional (2D) simulation domain with a size of $90 \times 90 \mu\text{m}^2$. Al-4 wt%Cu alloy is chosen to demonstrate the simulation scheme because the material has been widely used in many experimental studies. The physical properties of Al-4 wt% Cu alloy are listed in Table 1

The setup of the simulation domain is illustrated in Fig. 3. Four nuclei are manually placed at the bottom of the simulation domain. The locations of four nuclei are $x = 11.25 \mu\text{m}$, $33.75 \mu\text{m}$, $56.25 \mu\text{m}$, and $78.75 \mu\text{m}$, respectively. The zero Neumann boundary conditions are applied for all the variables at the walls. The no-slip boundary conditions are set at the solid-liquid interface for the liquid velocity \mathbf{u}_l . The electric potential and the normal component of electric current are continuous at the solid-liquid interface. In all simulation runs, the grid spacing of the simulation domain is $\Delta x = 0.3 \mu\text{m}$ for both x and y directions, and the time step is $\Delta t = 2 \times 10^{-7}$ s. The initial diameter of the seed is $D = 7 \Delta x$, and the width of the solid-liquid interface is $\eta = 5 \Delta x$. The initial temperature is $T = 920$ K. The initial composition of Cu in the liquid phase is $C_0 = 4$ wt% for the whole simulation domain.

Table 1
The physical properties of Al-4 wt%Cu alloy [22].

Properties	Symbol	Value
Melting point of pure Al	T_m [K]	933.6
Density of liquid	ρ [kg/m^3]	2700
Slope of liquidus	m_l [K/wt%]	-2.6
Partition coefficient	k	0.14
Density variation	$\frac{1}{\rho} \frac{\partial \rho}{\partial C}$ [1/%]	0.01 [46]
Thermal expansion coefficient	β_T [1/K]	1.17×10^{-4} [50]
Gravitational acceleration	g [m/s^2]	-9.8
Seebeck coefficient of solid	S_s [V/K]	-1.5×10^{-6} [16]
Seebeck coefficient of liquid	S_l [V/K]	-2.25×10^{-6} [16]
Electrical conductivity of solid	κ_s [S/m]	1.3×10^7 [53]
Electrical conductivity of liquid	κ_l [S/m]	3.8×10^6 [53]
Diffusivity of liquid	D_l [m^2/s]	3.0×10^{-9}
Prefactor of interfacial energy stiffness	σ_0^* [J/m^2]	0.24
Interfacial energy stiffness anisotropy	e^*	0.35
Kinematic viscosity	ν [m^2/s]	5.7×10^{-7}

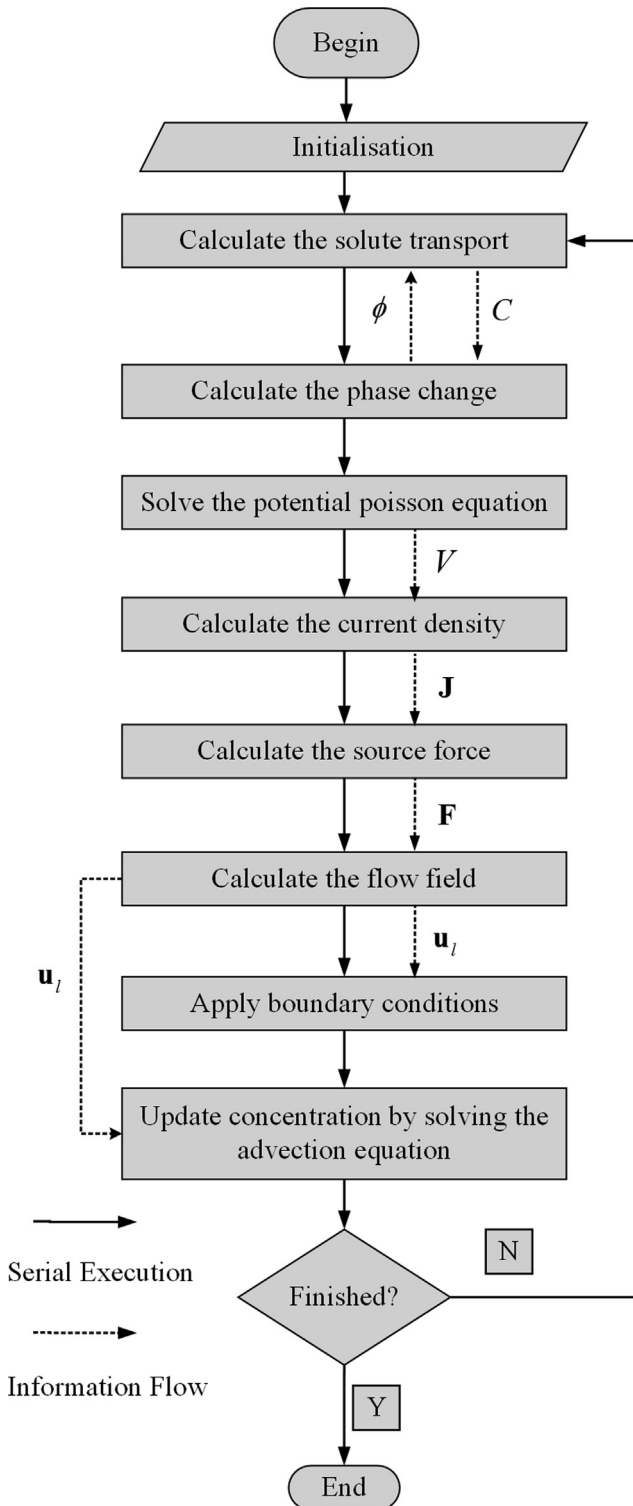


Fig. 2. The flowchart of the PF-MF-LBM simulation model.

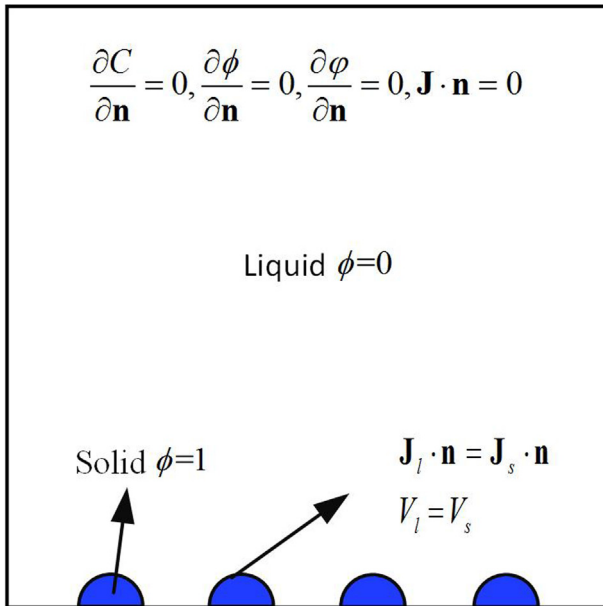


Fig. 3. The setup of boundary conditions.

In this example, the temperature in the simulation domain is assumed to be a one-dimensional (1D) temperature field with a constant thermal gradient. The temperature decreases linearly in time with a fixed cooling rate. The simplification of the temperature is based on the following observations. First, the thermal diffusivity $\alpha = 4.9 \times 10^{-5} \text{ m}^2/\text{s}$ is about four orders of magnitude larger than the solute diffusivity $D_l = 3 \times 10^{-9} \text{ m}^2/\text{s}$, which means that the heat transfer is much faster than the solute diffusion. Therefore, the temperature will reach the equilibrium state much more quickly than the composition. Second, the Péclet number for heat transfer is $Pe_L = Lu/\alpha$, where $L = 90 \text{ }\mu\text{m}$ is the feature size, $u = 10^{-3} \text{ m/s}$ is the magnitude of flow velocity, $\alpha = 4.9 \times 10^{-5} \text{ m}^2/\text{s}$ is the thermal diffusivity. Here, the Péclet number $Pe_L = 1.84 \times 10^{-3}$ is much smaller than unity, which means that the influence of melt convection on temperature distribution can be neglected. In addition, the complete thermal distribution and latent heat effect have been studied in our previous work [22,30], where the heat transfer phenomenon was simulated using TLBM to investigate the effect of nonlinear temperature field on the dendritic growth. The temperature field is simplified in this work to reduce the computational cost, since the goal here is to investigate the influence of TEMC on the dendritic growth and composition distribution. The solute redistribution induced by

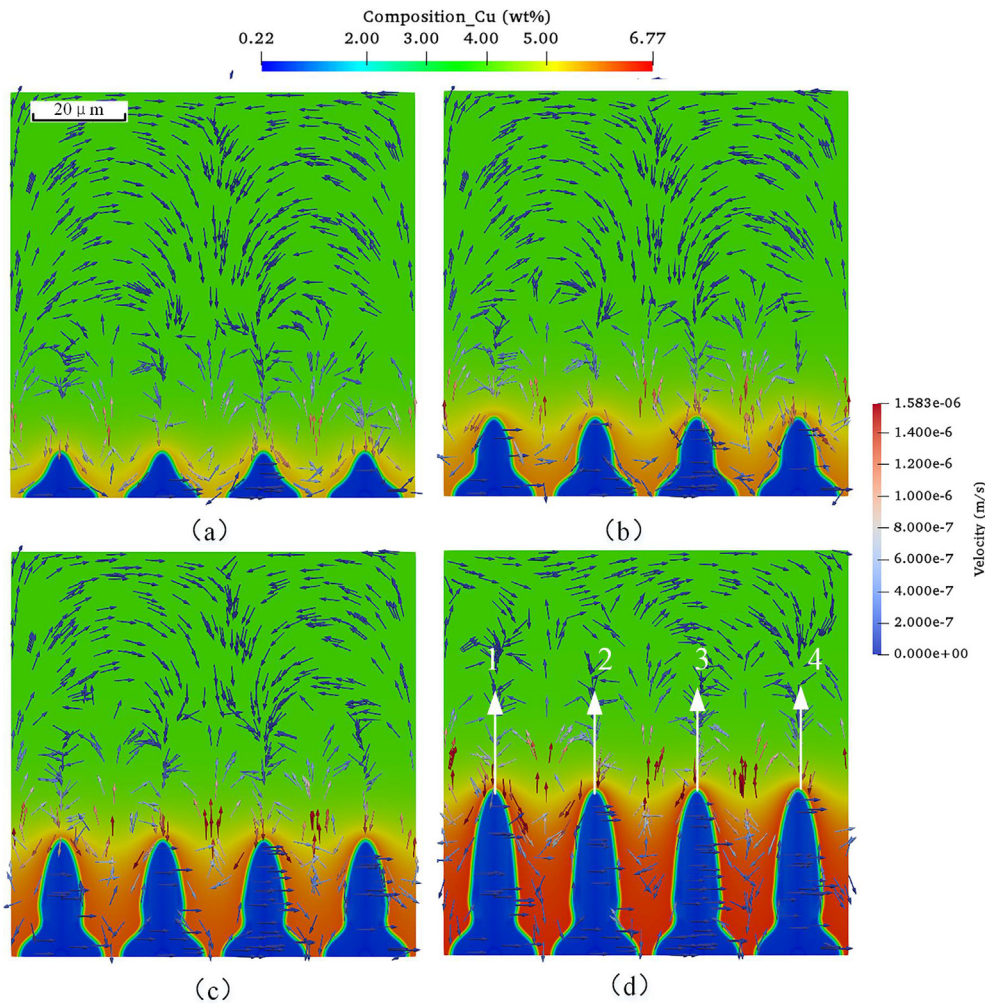


Fig. 4. The composition distribution and melt flow evolution with natural convection at (a) 20 ms, (b) 40 ms, (c) 60 ms, and (d) 80 ms. (The tip growth speed is 0.8 mm/s at $t = 80 \text{ ms}$.)

the TEMC has a significant influence on the dendritic growth. In order to show the TEMC effect more explicitly, the white noise in Eq. (19) is suppressed in this example as another simplification.

3.1.1. Dendritic growth with the buoyancy force

For comparison purpose, the dendritic growth without an external magnetic field is first simulated. The cooling rate is 40 K/s and a constant thermal gradient of 6000 K/m is applied. The amplitude of the noise is zero. Because the gravity is inevitable under terrestrial gravity conditions, the buoyancy force is considered in all simulations. The solute expansion coefficient of Al-Cu alloy is negative in Eq. (27), which means that the Cu-rich liquid is heavier than the Cu-poor liquid [54]. Fig. 4 shows the dendritic morphology and velocity field evolution at time $t = 20$ ms, 40 ms, 60 ms, and 80 ms with the natural convection, respectively. The arrows show the directions of flow velocities. Note that the colors of the arrows instead of the lengths indicate the magnitudes of the velocities. At the early stage, the dendrite tip grows fast, and the heavier copper is rejected at the front of the tips and sinks. The solutal difference induces natural convection flows, which results in a downward flow at each dendritic tip and both sides of each dendrite in the vicinity of the solid-liquid interface. The melt between the dendrites is also pushed upward due to the continuity of flows. As a result, circulatory flow vortices are formed. This flow pattern is similar to other simulation results in [46,54]. The vortex flows between dendrites are symmetrical. The shape of the dendrites is

also symmetrical. As the grain grows, the composition of copper at the solid-liquid interface increases, which makes the flow more intense.

3.1.2. Dendritic growth under an external magnetic field

To investigate the influence of TEMC on the dendritic growth and composition distribution, an external magnetic field of 0.5 T is applied in the simulation. The other parameters are the same as the case in Section 3.1.1. Fig. 5 shows the evolution of the dendritic morphology and velocity field. In Fig. 5(a), the dendrite is small at the initial stage of growth at $t = 20$ ms. Across the interface regions for all dendrites, there is a global flow from left to right at the solidification front, which is driven by the Lorentz force. The flow passes through the tips and interdendritic regions, changing its direction along the left and right sides of domain boundaries. The flow at the vicinity of the solid-liquid interface is intense and vanishes as it goes away from the interface. As a result of the magnetic field, the morphology of dendrites is no longer uniform, and the crystal is not symmetric. For each dendrite, the left half of the dendrite grows faster than the right half, because more rejected solute is carried away by the fluid flow. There is an upward flow at the left side of each dendrite and a downward flow at the right side. The upward flow takes away the rejected solute at the interface, whereas the downward flow contributes to the microsegregation. Therefore, the upward flow on the left promotes the growth of the secondary arms, whereas the downward flow on

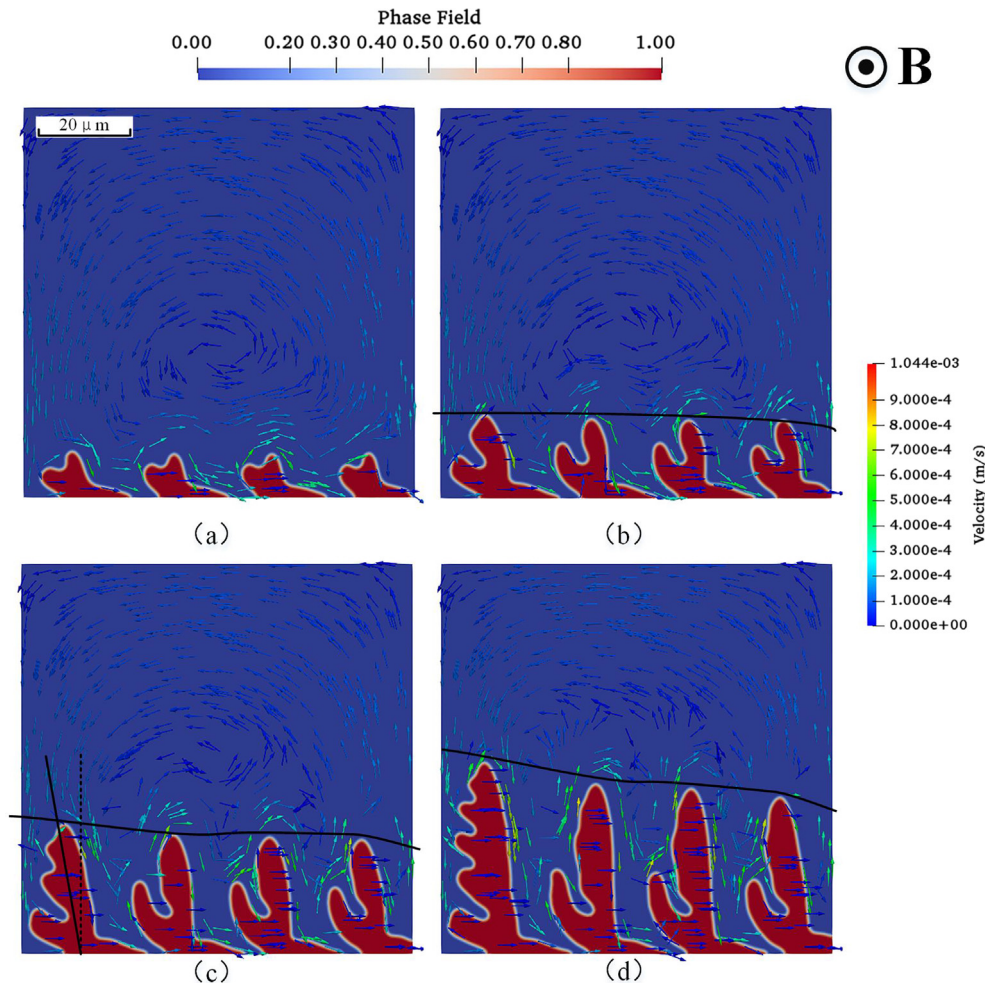


Fig. 5. The melt flow and dendrites evolution with a 0.5 T external magnetic field at (a) 20 ms, (b) 40 ms, (c) 60 ms, and (d) 80 ms. (The tip growth speed of the leftmost grain is 1.05 mm/s at $t = 80$ ms.)

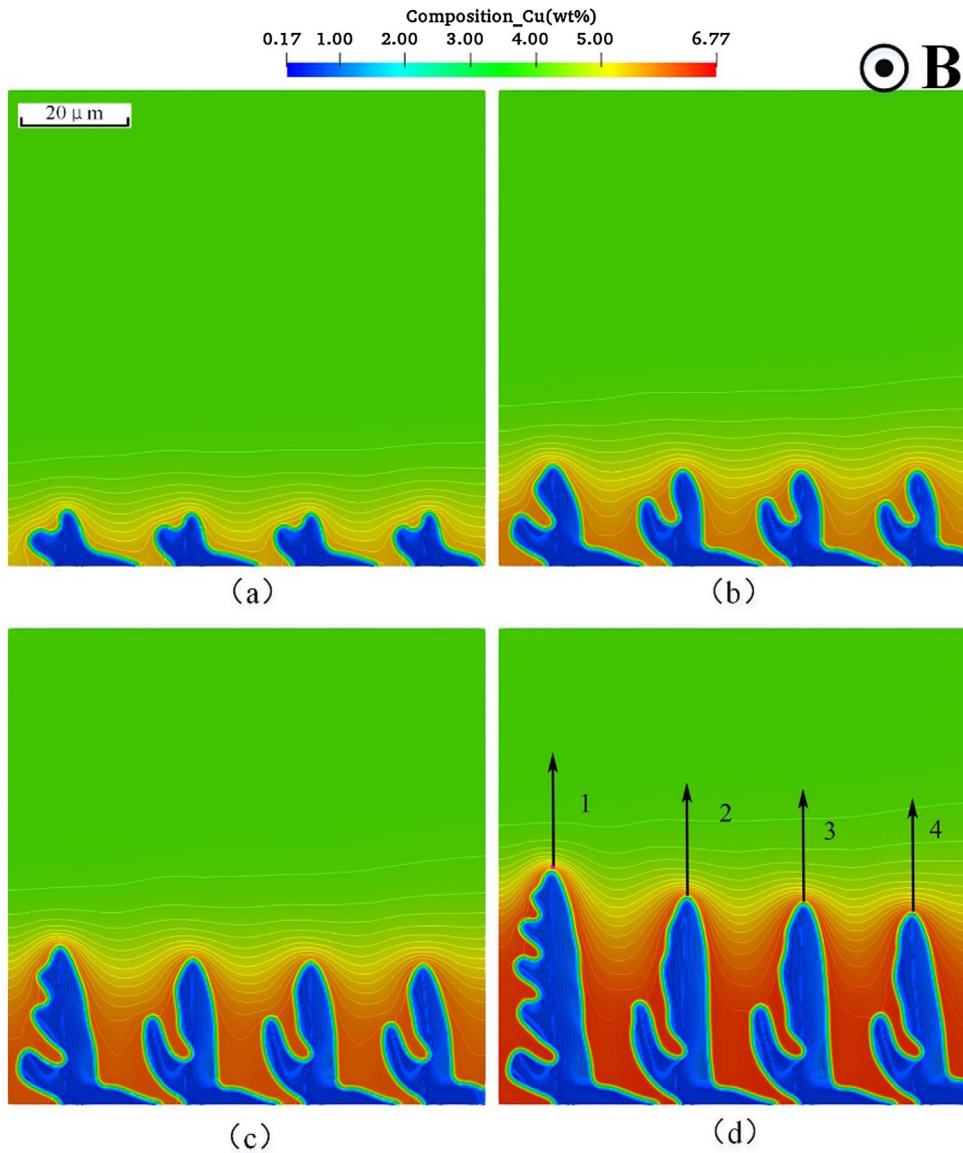


Fig. 6. The composition distributions with a 0.5 T external magnetic field at (a) 20 ms, (b) 40 ms, (c) 60 ms, and (d) 80 ms. (The contour lines indicate the isolines of the composition.)

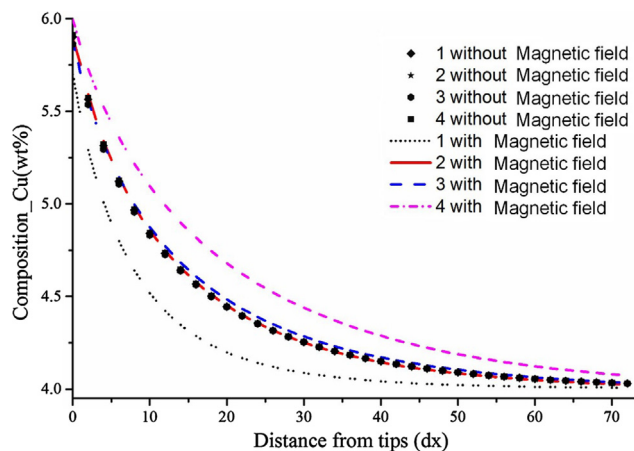


Fig. 7. The composition distribution along the lines in Fig. 6(d) and Fig. 4(d) at $t = 80$ ms with and without magnetic field.

the right suppresses the growth of the secondary arms. Small local vortices are also formed as the moving fluid encounters the dendrites.

Furthermore, the growth speed is asymmetric for each dendrite. As shown in Fig. 5(c), the primary trunk tilts toward the left, and the inclined angle increases as the dendrite grows. Because of the flow from left to right at the solidification front in the simulation domain, the intensity of microsegregation increases from left to right. This flow accelerates the growth of the dendrites at the upstream, which is the left side of the simulation domain, while the microsegregation suppresses the growth of dendrites at the downstream. As a result, the tip growth speed is not equal for different dendrites. As shown in Fig. 5(d), the growth speed of the left-most tip is 1.05 mm/s at $t = 80$ ms. The solidification front, indicated by the curve from left to right, gradually becomes tilted towards the right. The size difference between dendrites becomes more evident as they grow. The radius of the left-most tip is about 3 μm . The different levels of microsegregation can also be observed in Fig. 6, where the contour lines are the composition isolines. It is

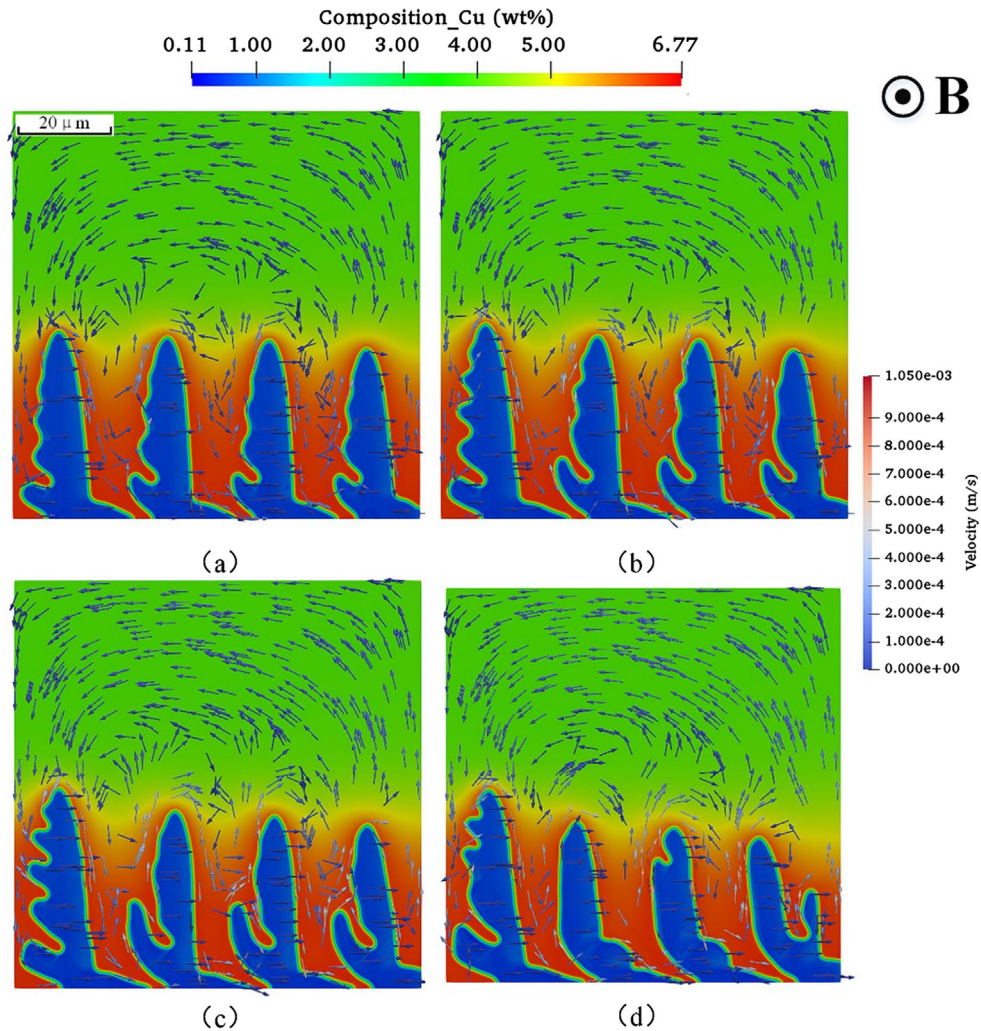


Fig. 8. The influence of magnetic field on velocity field and dendritic morphology, when the magnetic field density is (a) 0.1 T, (b) 0.3 T, (c) 0.5 T, and (d) 0.6 T at the time of 80 ms, respectively.

Table 2

The quantitative characterization of the influence of magnetic field.

Magnetic field intensity (T)	Maximum flow velocity (mm/s)	Flow direction	Dendritic tilt angle of the leftmost dendrite (°)
0	2.453×10^{-3}	Up and down	0
0.1	0.4372	Right	4.2
0.3	0.6394	Right	4.6
0.5	0.8343	Right	5.9
0.6	1.050	Right	6.7

seen that the microsegregation is uneven from the upstream to downstream. Compared to the natural convection, the TEMC induces much faster fluid flows. The maximum velocity under the magnetic field of 0.5 T is at least two orders of magnitude higher than the one without the magnetic field. Therefore, the external magnetic field can be an effective approach to suppress the natural convection.

Fig. 7 shows the composition distribution with and without the magnetic field along the vertical lines marked in Fig. 6(d) and Fig. 4(d) at $t = 80$ ms respectively. The indices 1 to 4 are the grain identification (IDs) from left to right. It is seen that without the magnetic field the composition of copper in the liquid region decreases at the same rate among the four tips, as it

moves away from the solid-liquid interface. In contrast, when the magnetic field is imposed, the rates of composition reduction among the four tips are different. The composition reduction is faster on the left side or upper stream, which makes the composition gradient larger. Therefore, the solute diffuses faster. The driving force on the left side of the domain is higher than that of the right side. Therefore, the tip growth velocities reduce gradually from left to right side.

3.1.3. The dendritic growth under different magnetic field intensities

To further study the influence of magnetic field density on the dendrite morphology, more simulation runs are conducted with different magnetic field intensities while the other parameters are the same as those in Section 3.1.1. Fig. 8 shows the dendrite morphology at $t = 80$ ms under different magnetic fields of 0.1 T, 0.3 T, 0.5 T, and 0.6 T, respectively. Compared to Fig. 4 without the magnetic field, the dendritic morphologies in Fig. 8 are significantly different. The crystals become increasingly asymmetric as the magnetic field intensifies. The dendritic interface also becomes smoother. The vortices are formed when the flow encounters dendrite arms. When the external magnetic field intensifies, the flow velocity increases, and the difference between the microsegregation levels in different local regions become more evident. Nevertheless, the flow velocity does not increase linearly with the

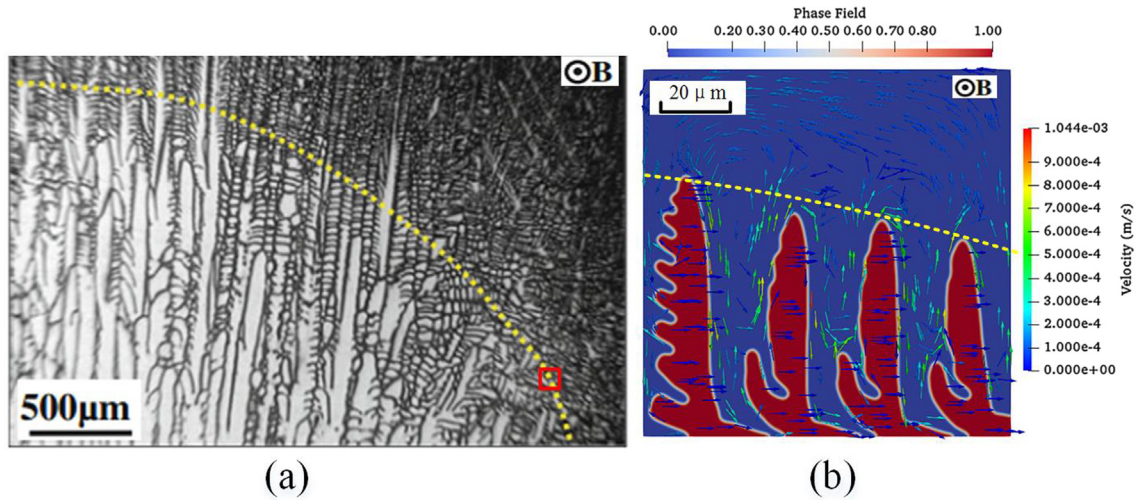


Fig. 9. The comparison between simulation and experiment. (a) the experimental result in Ref. [20] (courtesy of Wang et al.) and (b) the simulation result.

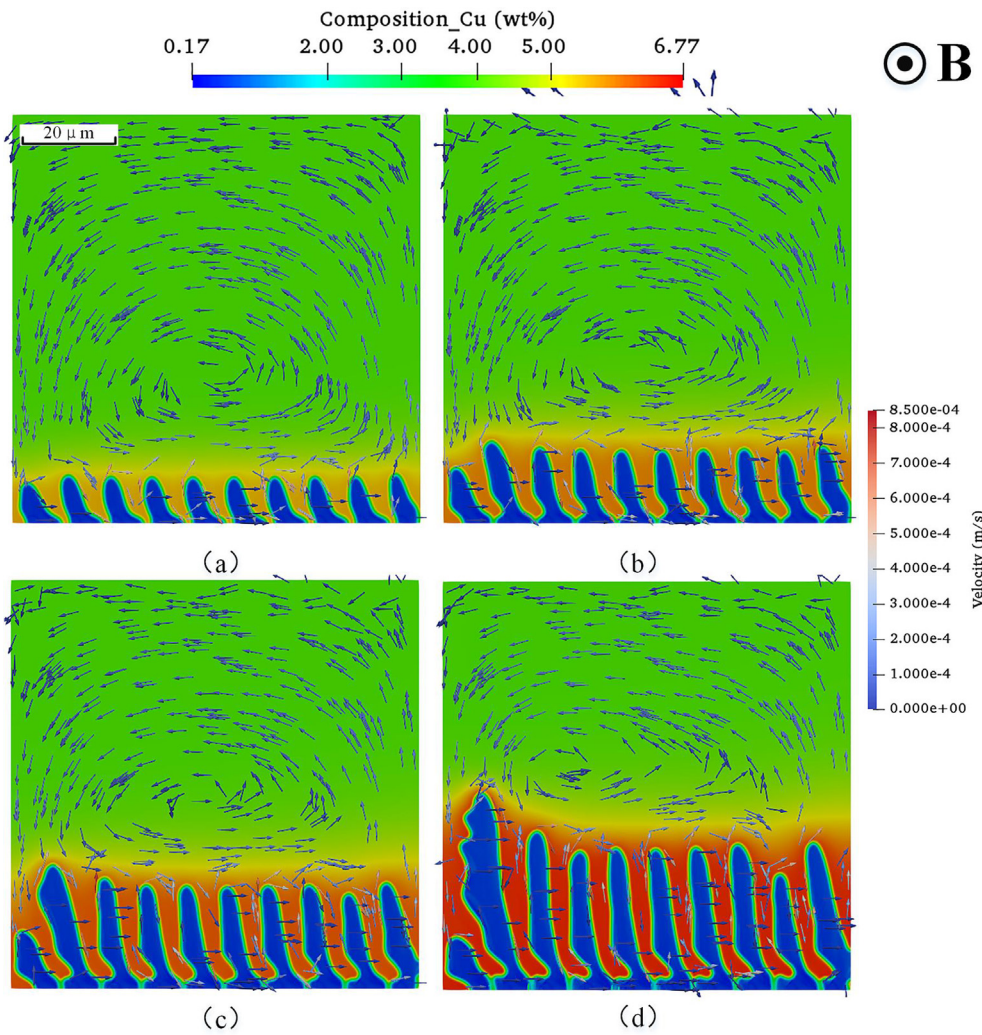


Fig.10. The composition distributions with a 0.5 T external magnetic field at different times. (a) 20 ms, (b) 40 ms, (c) 60 ms, and (d) 80 ms. (more dendrites are considered).

increase of the magnetic field. Other damping effects will dominate the fluid flow when the magnetic field density is very large [19]. To quantitatively characterize the effect of the magnetic field in the natural convection, the maximum flow velocity and dendritic tilt-

ing degree are obtained, which are listed in Table 2. It shows that the magnetic field induces strong fluid flows towards the right side. The maximum flow velocity and the dendritic tilt angle increase as the magnetic field intensifies.

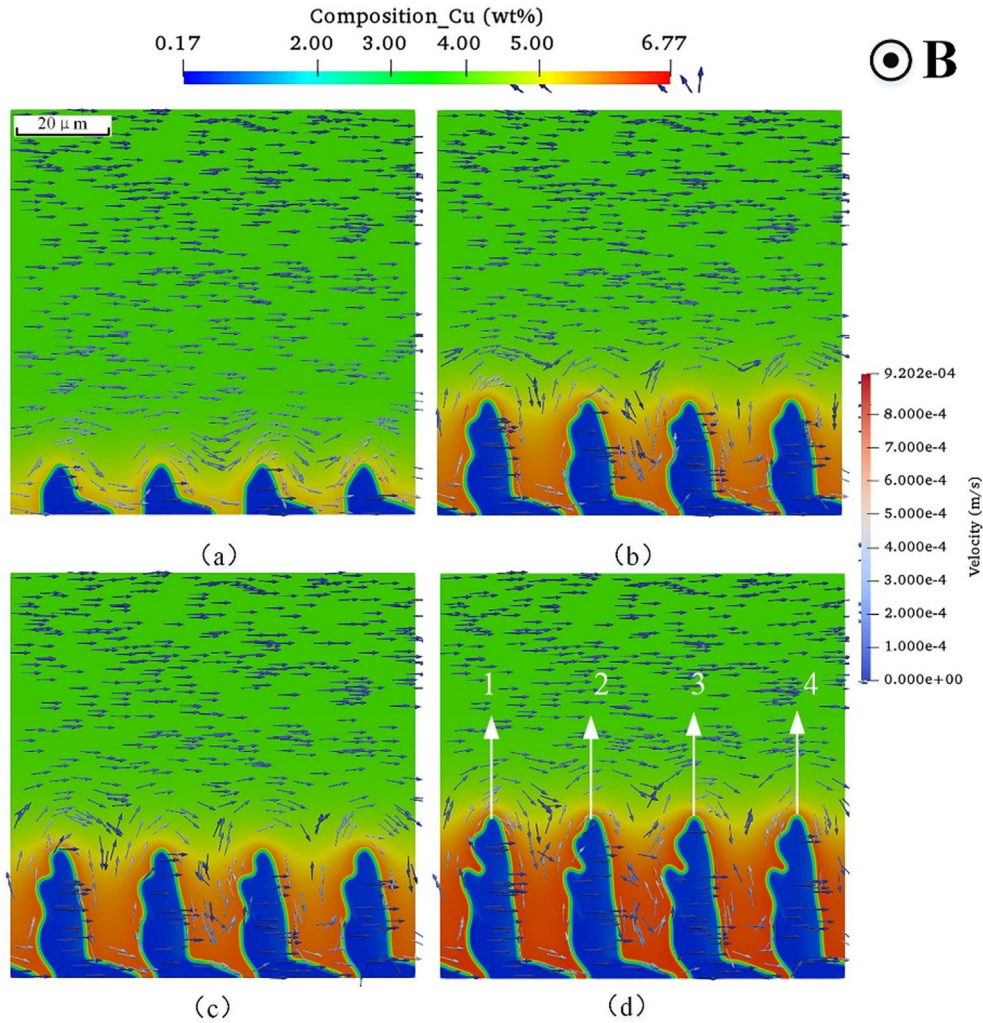


Fig. 11. The composition distributions evolution under a 0.5 T external magnetic field with periodic boundary for the side walls. (a) 20 ms, (b) 40 ms, (c) 60 ms, and (d) 80 ms.

3.1.4. Comparison with experimental observation

The simulated dendritic morphology under magnetic field is qualitatively compared with the experimental observation in Ref. [20]. The experimental result was obtained with Al-2.5 wt%Cu alloy with a thermal gradient of 6000 K/m and a magnetic field of 0.5 T. A water-cooled cylinder containing Ga-In-Sn liquid metal was used to cool down the samples in a process called liquid metal cooling. To preserve the morphology of the solid-liquid interface, quenching was carried out by quickly cooling the specimen down to the room temperature [20]. The quenched dendrites and the direction of the external magnetic field are shown in the optical microscopy image in Fig. 9(a), where the dendrites grow upward. The growth speeds of dendrite tips are not uniform under the influence of the external magnetic field. The dotted curve indicates the curved solidification front. As an illustration of the size of the simulated domain, a region of $90 \times 90 \mu\text{m}^2$ is marked by the rectangular box. The curved solidification front is also seen in the simulation result at $t = 100 \text{ ms}$ under a magnetic field of 0.5 T in Fig. 9(b), where the curved solidification front is also highlighted. It is observed that the solidification front gradually becomes tilted towards the right because the melt flow caused by the TEMC, which leads to the solute accumulation near the right wall and the suppression of the dendritic growth. The simulation result qualitatively matches the experimental observation of the curved solidification front.

Because phase field simulation is prohibitively expensive to simulate the solidification of large systems, only a small domain is simulated in this example. Nevertheless, the simulation has revealed the TEMC effects on dendritic morphology and composition distribution. Note that the intensified fluid flow exhibits more

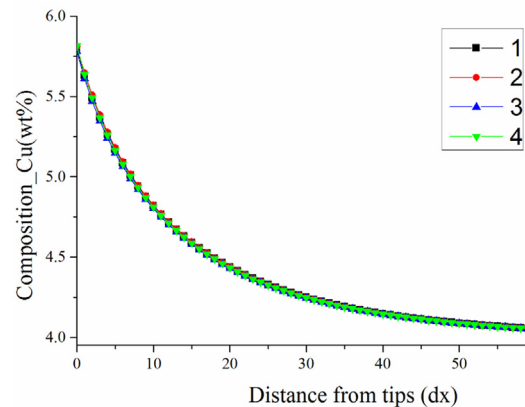


Fig. 12. The composition distribution at the tips along the lines in Fig. 3(d) at $t = 80 \text{ ms}$.

prominent effects in small simulation domains than those in larger ones, because the TEMC causes the global circulation. Small simulation domains in the scale of $100\ \mu\text{m}$ are still valid for small melt pools such as those in the selective laser melting process. A second challenge in phase field simulation of solidification is the time scale. It is computationally expensive to obtain completely solidified grains in detailed phase field simulation, especially for casting process with relatively small thermal gradients and cooling rates. Our simulation still reveals the unique flow pattern as a result of the TEMC and elucidates the cause of the observed microstructure.

3.1.5. The influence of dendritic number and side wall

To study the influence of dendritic number and side wall on the dendritic morphology, we also performed sensitivity analysis on the dendritic number and side boundary condition. More initial dendritic seeds were added at the bottom boundary and the boundary condition is the same. The simulation result is shown in Fig. 10. The fluid momentum induced by the external magnetic field flows from the left to the right. The solute was transported to the right side of the domain. The different levels of microsegregation are also observed. The dendritic growths near the left and right sides are affected more than the one in the middle. The dendrites in the middle grow at a similar speed. To further show the side wall effect, in a different simulation, periodic boundary conditions are set for the side walls, which simulates a melt pool with an infinite size. The result is shown in Fig. 11. It is seen that there is no curved solidification front any more. All dendrites grow at the similar speed. However, the asymmetric dendritic morphology caused by the magnetic field still exist. Fig. 12 shows the composition distribution along the vertical lines marked in Fig. 11 (d). It is seen that the content of copper in the liquid region decreases at almost the same rate among the four tips, as it moves away from the solid-liquid interface. The composition gradient at the tips is the same, therefore the driving force is similar.

The simulation results show that the magnetic field induced flows affect the dendritic growth in two ways. The larger vortices affect the tip growth speed such as in the boundary region, whereas smaller and local vortices between dendrites affect the shapes of dendrites. For a melt pool with a finite size, there is always a side wall effect. To simulate a melt pool with the finite size, it is reasonable to adopt the zero Neumann boundary condition.

3.2. Simulation of magnetic field assisted laser welding

In the second example, the magnetic field assisted laser welding is simulated. To validate the simulation results, laser welding experiments were conducted with and without the influence of the magnetic field. The schematic diagram of the welding experiment is shown in Fig. 13(a). An external magnetic field of 0.4 T is applied during the welding experiment, which is perpendicular to the welding direction and the surface of the Al-Cu workpiece. The laser beam is tilted about 8 degrees along the welding direction. The laser power is 2.5 kW and the welding speed is 2 m/min. The size of the workpiece is $100 \times 50 \times 4\ \text{mm}^3$. The metallographic samples were cut from the welded workpiece using an electric discharge machine. The top surface of the samples was chosen to test. To avoid the influence of oxidation, a thickness of 0.1 mm below the top surface was polished. As shown in Fig. 13 (b), the simulation domain is regarded as a small corner of the melt pool. The inputs for the simulation include the thermal gradient and the cooling rate. However, during the laser welding, the accurate cooling rate and the thermal gradient are difficult to obtain. Therefore, a verified macro finite volume method (FVM) model in our previous work [55] was used to simulate the welding process

and estimate the cooling rate and thermal gradient. Similar to the work by Farzadi et al. [56], the FVM model was used to obtain the temperature distribution in the weld pool. The average temperature gradient and cooling rate along the fusion boundary were obtained by tracking the calculated temperature profiles. The calculated average cooling rate and thermal gradient from the FVM model are $2 \times 10^5\ \text{K/m}$ and $1000\ \text{K/s}$.

During the solidification simulation, it is assumed that at the boundary between the mushy zone and weld pool the solidification mode transforms from the planar growth to dendritic growth due to perturbation. The direct effect of the perturbation is the formation of nuclei at the boundary. The stochastic thermal noise introduced in Eq. (22) is taken with the amplitude $A = 0.001$. Fig. 14 and Fig. 15 show the velocity field and dendritic morphology evolution with and without the magnetic field during laser welding, respectively. The dendrites grow upward. The downward natural convection is weak and the dendritic morphologies are symmetrical without the magnetic field. When the magnetic field is imposed, a strong fluid flow from left to right dominates, and the dendritic morphologies are no longer uniform.

Fig. 16 shows the comparison of composition distributions between our simulation predictions and experimental measurements. Fig. 16 (a) shows the microstructure in the SEM image without the magnetic field, and Fig. 16 (b) shows the microstructure in the SEM image with a 0.4 T external magnetic field. An ideal situation for model validation is to directly compare the simulated grain evolution including the number, size, and shape of dendritic branches with the ones observed in experiments. However, there are several technical barriers. First, there is a lack of in-situ experimental measurement methods to directly observe the dendritic growth in rapid solidification because of time-scale and length-scale limitations, even though there have been on-going research efforts. The images taken after the solidification process do not

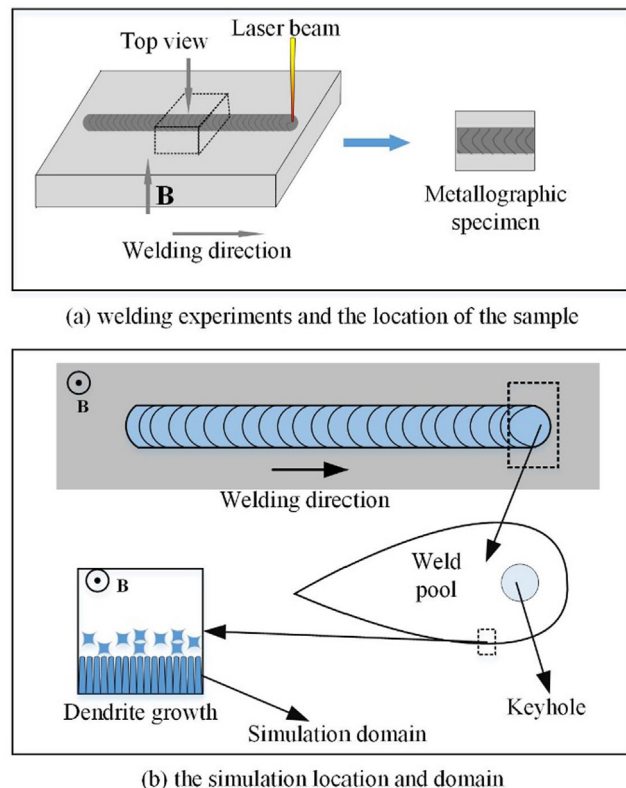


Fig. 13. Schematic diagram of the welding experiment and the simulation domain.

show the dendritic branches either. They can only show the grain morphology after the solidification is completed and solid-state phase transformation which is common in alloys is finished. Second, phase-field method to simulate the complete solidification process requires a very long computational time, especially when latent heat and thermal effects are considered. The complete solidification of the final liquid trapped between grains will take exponentially longer time than the initial solid interface growth. So there is a mismatch of time scales in simulating rapid solidification. Third, even if we have in-situ experimental measurement of dendritic morphologies and simulated ones, they are stochastic in nature as a result of many uncontrollable factors. Quantitative metrics need to be developed for validation. Given the above challenges of comparing morphologies, in this work, we propose to use composition as the metric for quantitative validation. When solidification in a local region is nearly finished, even with a small amount of liquid trapped, its composition should be very similar to the final solid when the solidification is completed. The information of composition distribution is also very valuable, which determines important mechanical and chemical properties of solidified structures. Therefore, composition is a good quantitative metric to compare directly.

The distribution of Cu concentration is used for quantitative comparison here. The concentration of Cu along lines A and B in Fig. 16 (a) and (b) was measured by electron probe microanalysis (EPMA) with a sampling interval of $0.3 \mu\text{m}$. Fig. 16 (c) shows the measured wt% of Cu along the two lines with and without the magnetic field. Fig. 16 (d) shows the simulated composition along the

lines in Fig. 14(d) and Fig. 15(d). The x-axis is the distance to the starting point. The y-axis is the wt% of Cu. The variations of composition along the lines are clearly seen. The Cu concentration is higher at the solid-liquid interface because of microsegregation. The fluctuation patterns with and without magnetic field are different. To quantify the difference, a spectrum analysis of the distribution in Fig. 16 (c) and (d) was conducted by applying the one-dimensional Fast Fourier Transformation (FFT). As shown in the frequency spectrum in Fig. 17, the x-axis is the spatial frequency and the y-axis is the amplitude. The spatial frequency is a measure of how often sinusoidal components (as determined by the Fourier transform) of the structure repeat per unit of distance. When the external magnetic is imposed, the number of peaks increases and the peak values are lower. This means that the external magnetic field helps to promote the growth of secondary arms and reduce the microsegregation. The integrations of the amplitude or the accumulative amplitudes along the spatial frequency after normalization are calculated and shown in Fig. 18. It is seen that there is a shift of amplitudes towards high frequencies for both simulation and experimental measurement when the external magnetic field is imposed, because the magnetic field intensifies the flow and makes the solute distribution more heterogeneous. In other words, more dendritic branches are formed after the magnetic field is imposed. Simulation results show the same effect of magnetic field as the experimental observation.

A deviation in the accumulative amplitude can be observed between the simulation and experimental results. There can be

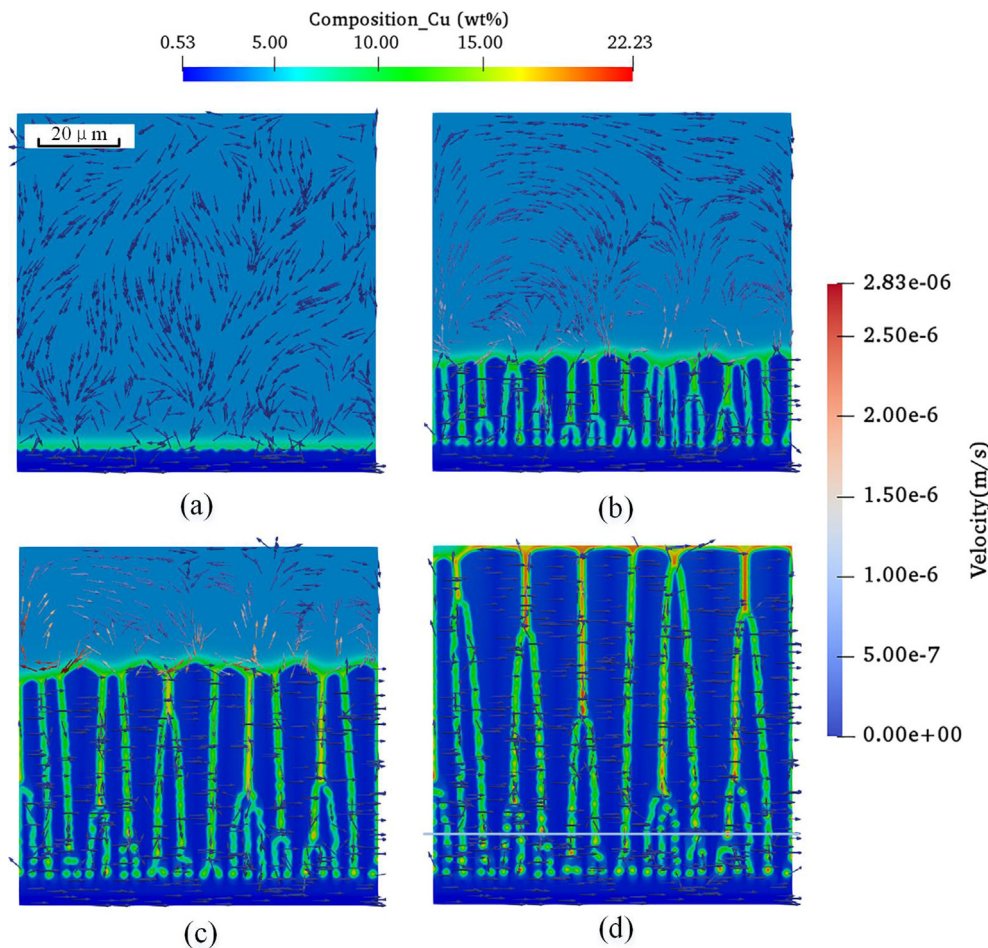


Fig. 14. The dendritic morphology evolution at the melt boundary without the magnetic field during laser welding. (a) 2 ms, (b) 8 ms, (c) 20 ms, and (d) 24 ms.

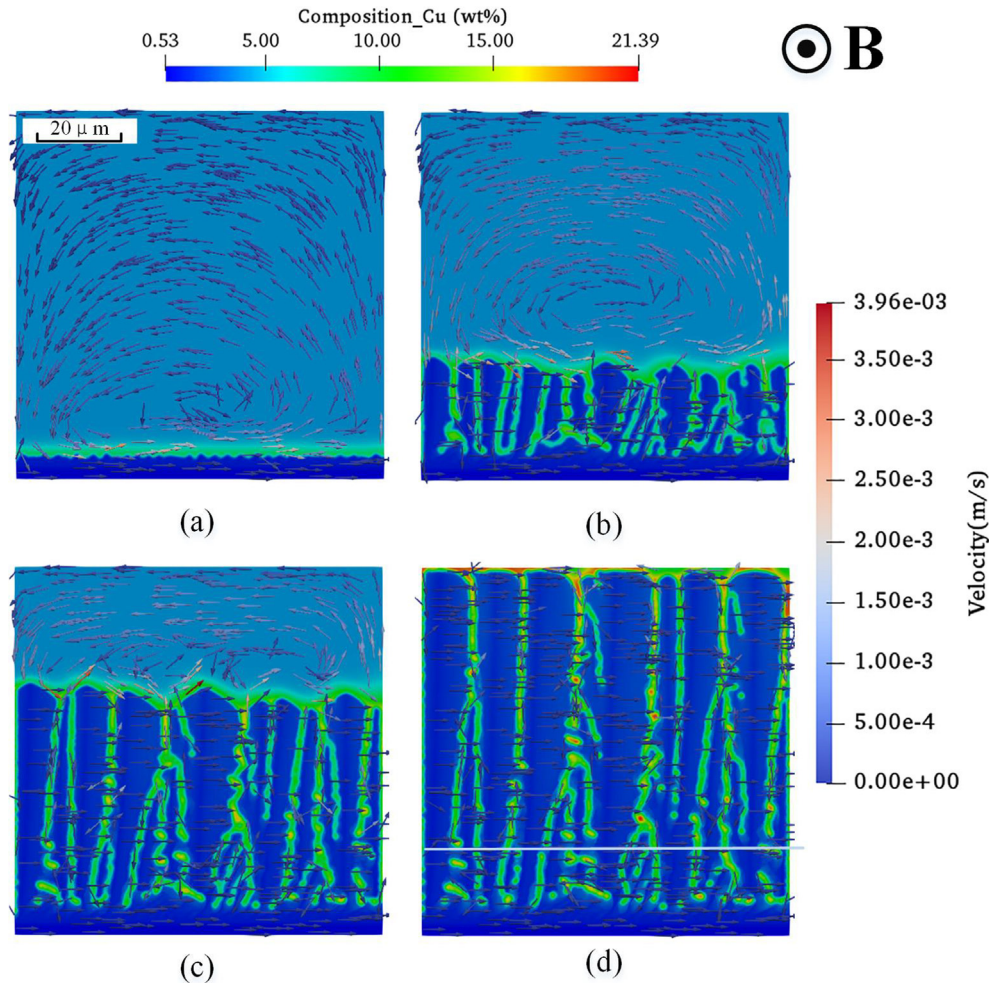


Fig. 15. The dendritic morphology evolution at the melt boundary under the influence of a magnetic field of 0.4 T during laser welding. (a) 2 ms, (b) 6 ms, (c) 24 ms, and (d) 36 ms. (the velocity of the tip close to left is 2.75 mm/s at $t = 36$ ms).

several causes of this deviation. First, there are several sources of uncertainty in our model that potentially introduce errors. The nucleation process in the current model is based on stochastic thermal noises. A more accurate first-principles nucleation model can be introduced to better predict the density of nuclei. Second, due to the limitation of computation, the simulation domain is much smaller than the actual weld pool and is restricted to two-dimensional. The small simulation domain introduces bias in the prediction of composition distribution. The affordable simulation time does not allow the simulated domain to be completely solidified. In laser welding, after the molten pool is completely solidified, solid-phase diffusion and solid state transition can occur, which will influence the composition distribution. Third, the one-dimensional samples taken from both experiments and simulations provide incomplete information of the two-dimensional stochastic distribution of composition. Two-dimensional probabilistic distributions obtained from multiple runs of simulations and samples of experiments will provide more complete information, but with higher computational and experimental costs. Due to the complexity of the solidification, the experimental measurements are also sensitive to the sampling position and interval. Furthermore, various approximations and numerical solutions of partial differential equations in phase field simulation introduce additional model form uncertainty, including truncation error, empirical treatment to eliminate numerical instability, and solid-liquid interface thickness overestimation. The numerical errors are common and inevitable for numerical simula-

tions. Among the above causes, the error associated with the nucleation model is the most important one because the density of nuclei has a distinct effect on the dendritic number, morphology, and the composition distribution. The second most important error source is the limited computational resource. The third one is the experimental measurement. Overall, the study of quantitative model validation for phase field simulation of rapid solidification is still very limited and deserves more attentions. Our proposed validation approach based on the composition distribution is the first of its kind and hopefully stimulates more future research in quantitative validation.

4. Conclusion

In this paper, a multi-physics PF-MF-LBM model is developed to simulate the directed solidification process under the influence of external magnetic field. The dendritic growth, Seebeck effect, solute transport, solutal buoyancy, and thermoelectric magnetohydrodynamics are coupled in the new model. The phase field method is used to simulate the dendritic growth, while the Poisson equation and Ohm's law model the electromagnetic effect. The lattice Boltzmann method is applied to simulate solute convection and thermoelectric magnetohydrodynamics flows.

The simulation reveals the complex details of flows, solute composition, and dendritic growth during the solidification process. It

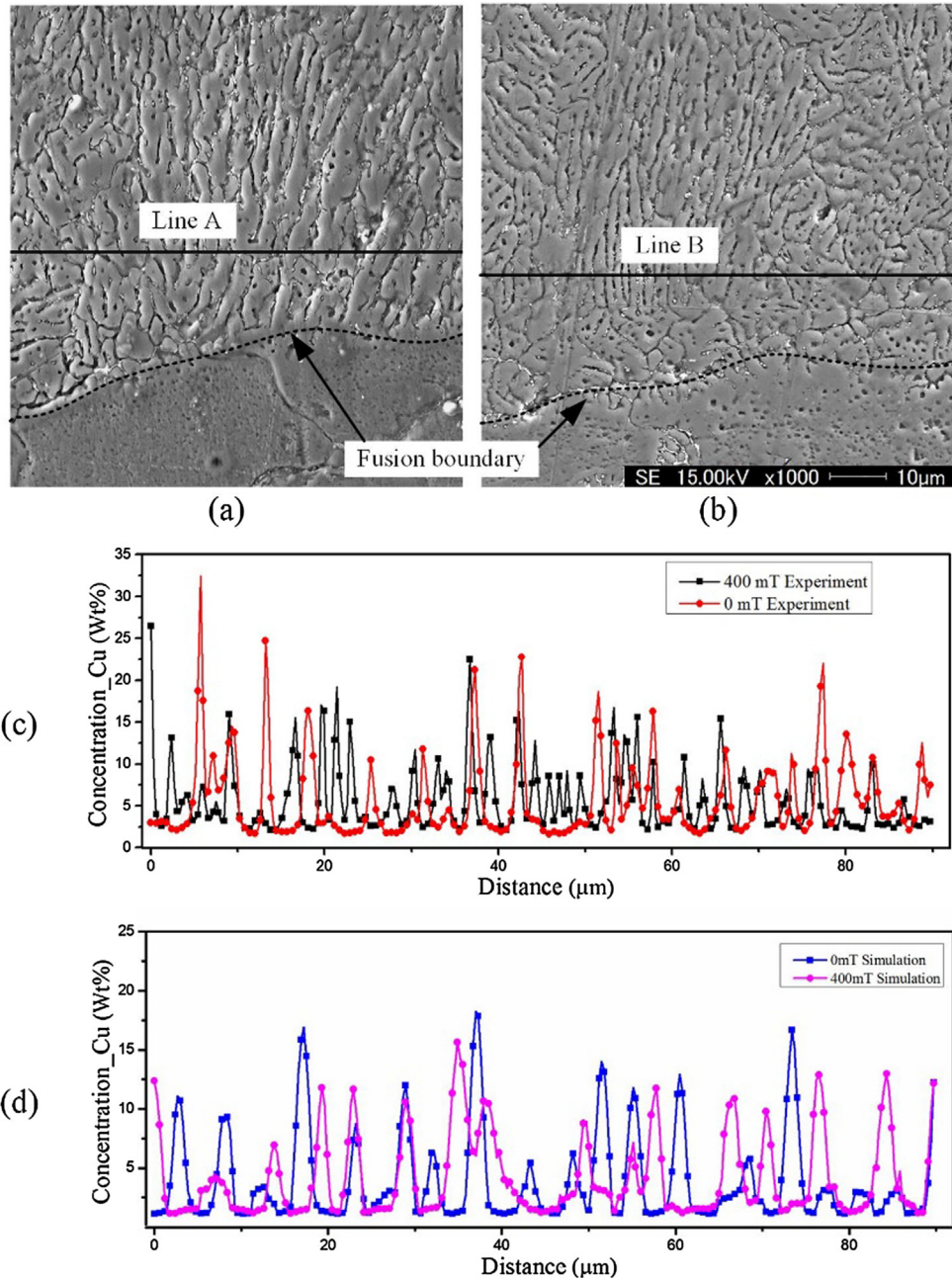


Fig. 16. The comparison of (a) the microstructure without magnetic field and (b) the microstructure with the magnetic field, (c) the comparison of composition distribution along the lines marked in (a) and (b), and (d) the comparison of composition distribution in simulation cases (thermal gradient is 2×10^5 K/m and the cooling rate is 1000 K/s).

is seen that the melt flow driven by the Lorentz force is concentrated in the vicinity of the solid-liquid interface, which leads to the uneven distribution and accumulation of solute locally in the downstream regions. The global flow suppresses the dendritic growth in those solute-rich regions. As a result, a curved solidification front is formed. The dendritic trunks are tilted because of the inhomogeneous growth on two sides of dendrites. Vortices are formed in the dendritic network because the flowing fluid is confined by side branches and primary arms, which has an influence on the side branch morphology. The curved solidification front and tilted primary trunks are unique phenomena in the magnetic field assisted directional solidification. Simulations show that the magnetic field can change the natural convection effectively. A

properly designed magnetic field can potentially reduce the defects caused by natural convection.

Methods for quantitative model validation in rapid solidification simulations are needed. In this work, a validation method based on composition is demonstrated. The comparison shows the consistency between our model predictions and experimental measurements, especially the effect of thermoelectromagnetic convection. Further quantitative analyses are needed, which may include direct measurements of thermoelectric current during dendritic growth and in-situ observation of dendritic growth. Direct measurements of composition distribution, velocity distribution, and other physical quantities will be helpful to better understand the directional solidification process. Yet there is still

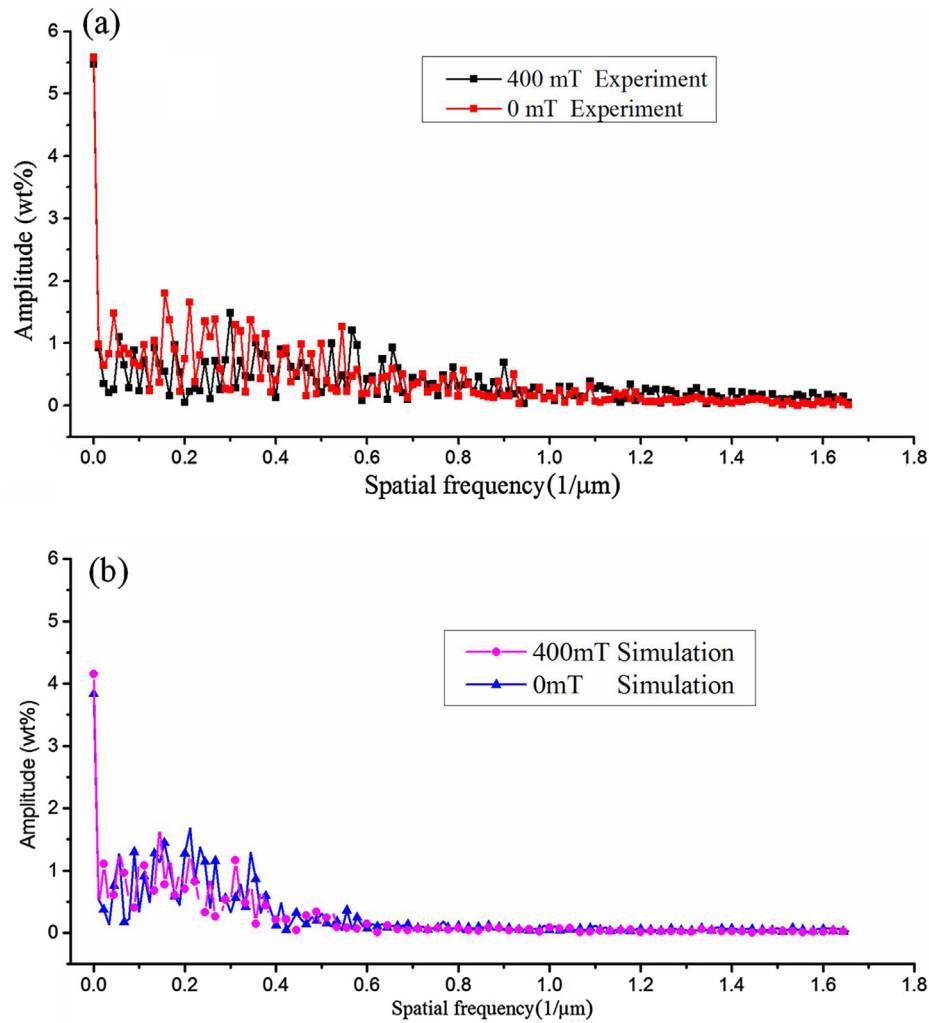


Fig. 17. The FFT analysis of (a) experimental and (b) simulation results.

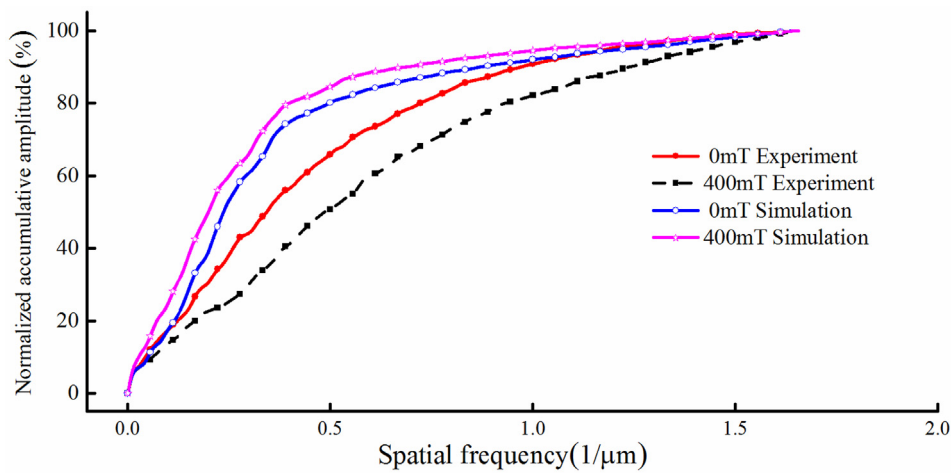


Fig. 18. The comparison of the accumulative Cu concentrations along spatial frequency between experiment and simulation.

a lack of in-situ experimental observation techniques for rapid solidification in laser welding and melting.

In future work, the proposed simulation model can also be extended by considering more factors, such as the release of latent heat, Peltier effect, and nucleation, so that the fidelity of

the model is further increased. By integrating our recently developed process optimization [57] and uncertainty quantification methods [58], we can establish more robust process-structure relationships to design and optimize the magnetic field assisted solidification process.

Declaration of Competing Interest

None.

Acknowledgements

This work was supported in part by the Open Research Foundation of the State Key Laboratory of Digital Manufacturing Equipment & Technology at Huazhong University of Science and Technology (grant No. DMETKF2018001) and the National Natural Science Foundation of China (grant No. 51721092).

References

- [1] L. Zhang, S. Wang, A. Dong, J. Gao, L.N.W. Damoah, Application of Electromagnetic (EM) separation technology to metal refining processes: A review, *Metall. Mater. Trans. B* 45 (6) (2014) 2153–2185.
- [2] Z.H.I. Sun, M. Guo, J. Vleugels, O. Van der Biest, B. Blanpain, Strong static magnetic field processing of metallic materials: A review, *Curr. Opin. Solid. St. M.* 16 (5) (2012) 254–267.
- [3] Q.A. Wang, T. Liu, K. Wang, C.J. Wang, K. Nakajima, J.C. He, Solidified structure control of metallic materials by static high magnetic fields, *Isij Int.* 50 (12) (2010) 1941–1946.
- [4] M.H. Avnaim, B. Mikhailovich, A. Azulay, A. Levy, Numerical and experimental study of the traveling magnetic field effect on the horizontal solidification in a rectangular cavity part 1: Liquid metal flow under the TMF impact, *Int. J. Heat Fluid Flow* 69 (2018) 23–32.
- [5] H. Liu, W. Xuan, X. Xie, C. Li, J. Wang, J. Yu, X. Li, Y. Zhong, Z. Ren, Columnar-to-equiaxed transition and equiaxed grain alignment in directionally solidified Ni₃Al alloy under an axial magnetic field, *Metall. Mater. Trans. A* 48 (9) (2017) 4193–4203.
- [6] M. Yao, A. Chait, A.L. Fripp, W.J. Debnam, Magnetically damped convection and segregation in Bridgman growth of PbSnTe, *J. Cryst. Growth* 173 (3–4) (1997) 467–480.
- [7] M. Bachmann, V. Avilov, A. Gumenyuk, M. Rethmeier, Numerical assessment and experimental verification of the influence of the Hartmann effect in laser beam welding processes by steady magnetic fields, *Int. J. Therm. Sci.* 101 (2016) 24–34.
- [8] L. Li, C. Ban, X. Shi, H. Zhang, Y. Zuo, Q. Zhu, X. Wang, J. Cui, H. Nagaumi, Influence of a high magnetic field on the solidification structures of ternary Al-Fe-Zr alloy, *J. Mater. Res.* 32 (11) (2017) 2035–2044.
- [9] H. Morikawa, K. Sassa, S. Asai, Control of precipitating phase alignment and crystal orientation by imposition of a high magnetic field, *Mater. Trans., JIM* 39 (8) (1998) 814–818.
- [10] J. Virbulis, T. Wetzels, A. Muiznieks, B. Hanna, E. Dornberger, E. Tomzig, A. Muhlbauer, W. von Ammon, Numerical investigation of silicon melt flow in large diameter CZ-crystal growth under the influence of steady and dynamic magnetic fields, *J. Cryst. Growth* 230 (1–2) (2001) 92–99.
- [11] A.E. Mikelson, Y.K. Karklin, Control of crystallization processes by means of magnetic fields, *J. Cryst. Growth* 52 (1981) 524–529.
- [12] J.S. Walker, A. Cröll, F.R. Szofran, Thermoelectromagnetic convection in floating zone silicon growth with a nonaxisymmetric temperature and a strong axial magnetic field, *J. Cryst. Growth* 223 (1–2) (2001) 73–82.
- [13] R. Moreau, O. Laskar, M. Tanaka, D. Camel, Thermoelectric magnetohydrodynamic effects on solidification of metallic alloys in the dendritic regime, *Mater. Sci. Eng., A* 173 (1–2) (1993) 93–100.
- [14] X. Li, Y. Fautrelle, Z. Ren, Influence of thermoelectric effects on the solid-liquid interface shape and cellular morphology in the mushy zone during the directional solidification of Al-Cu alloys under a magnetic field, *Acta Mater* 55 (11) (2007) 3803–3813.
- [15] I. Kaldre, Y. Fautrelle, J. Etay, A. Bojarevics, L. Buligins, Thermoelectric current and magnetic field interaction influence on the structure of directionally solidified Sn-10wt.%Pb alloy, *J. Alloy Compd.* 571 (2013) 50–55.
- [16] J. Wang, Y. Fautrelle, H. Nguyen-Thi, G. Reinhart, H. Liao, X. Li, Y. Zhong, Z. Ren, Thermoelectric magnetohydrodynamic flows and their induced change of solid-liquid interface shape in static magnetic field-assisted directional solidification, *Metallur. Mater. Trans. A* 47 (3) (2015) 1169–1179.
- [17] A. Kao, B. Cai, P.D. Lee, K. Pericleous, The effects of thermoelectric magnetohydrodynamics in directional solidification under a transverse magnetic field, *J. Cryst. Growth* 457 (2017) 270–274.
- [18] J.A. Shercliff, Thermoelectric magnetohydrodynamics, *J. Fluid Mech.* 91 (02) (1978) 231.
- [19] Y. Fautrelle, H. Nguyen-Thi, G. Salloum Abou Jaoude, G. Reinhart, N. Mangelinck-Noël, I. Kaldre, Thermoelectric magnetic flows in melt during directional solidification, *Appl. Phys. Lett.* 104 (12) (2014) 121916.
- [20] J. Wang, Z. Ren, Y. Fautrelle, X. Li, H. Nguyen-Thi, N. Mangelinck-Noel, G.S.A. Jaoude, Y. Zhong, I. Kaldre, A. Bojarevics, Modification of liquid/solid interface shape in directionally solidifying Al-Cu alloys by a transverse magnetic field, *J. Mater. Sci.* 48 (1) (2012) 213–219.
- [21] Y.D.T. Couvat, A. Gagnoud, D. Brasiliano, O. Budenkova, Y. Fautrelle, Numerical modelling of thermoelectric magnetic effects in solidification, in: 8th International Conference on Electromagnetic Processing of Materials, Oct 2015, Cannes, France. EPM2015 proceedings (2015).
- [22] D. Liu, Y. Wang, Mesoscale multi-physics simulation of solidification in selective laser melting process using a phase field and thermal lattice Boltzmann model, in: ASME 2017 International Design Engineering Technical Conferences and Computers and Information in Engineering Conference, American Society of Mechanical Engineers, Cleveland, Ohio, USA, 2017, pp. V001T002A027.
- [23] I. Steinbach, Phase-field models in materials science, *Modell. Simul. Mater. Sci. Eng.* 17 (7) (2009) 073001.
- [24] H. Xing, X.L. Dong, C.L. Chen, J.Y. Wang, L.F. Du, K.X. Jin, Phase-field simulation of tilted growth of dendritic arrays during directional solidification, *Int. J. Heat Mass Transf.* 90 (2015) 911–921.
- [25] M. Tegeler, O. Shchyglo, R.D. Kamachali, A. Monas, I. Steinbach, G. Sutmann, Parallel multiphase field simulations with OpenPhase, *Comput. Phys. Commun.* 215 (2017) 173–187.
- [26] D. Medvedev, F. Varnik, I. Steinbach, Simulating mobile dendrites in a flow, *Procedia Comput. Sci.* 18 (2013) 2512–2520.
- [27] Z.K. Feng, Y. Hong, G. Wang, X.H. Wu, D.C. Zeng, Effects of external magnetic field on the solidification process in Nd-Fe-B alloy: phase-field simulation, *Modell. Simul. Mater. Sci. Eng.* 26 (2) (2018) 025012.
- [28] H. Chang, C. Huang, B. Tang, R. Hu, J. Li, H. Zhong, Effect of a strong magnetic field on dendritic growth of Ti-Ni alloy, *Mater. Sci. Forum* (2013) 810–817.
- [29] A. Zhang, J. Du, Z. Guo, Q. Wang, S. Xiong, A phase-field lattice-boltzmann study on dendritic growth of Al-Cu alloy under convection, *Metallur. Mater. Trans. B* 49 (6) (2018) 3603–3615.
- [30] D.H. Liu, Y. Wang, Mesoscale multi-physics simulation of rapid solidification of Ti-6Al-4V alloy, *Addit. Manuf.* 25 (2019) 551–562.
- [31] T. Krüger, H. Kusumaatmaja, A. Kuzmin, O. Shardt, G. Silva, E.M. Viggien, *The Lattice Boltzmann Method: Principles and Practice*, Springer International Publishing, Switzerland, 2017.
- [32] T. Inamura, M. Yoshino, H. Inoue, R. Mizuno, F. Ogino, A Lattice Boltzmann method for a binary miscible fluid mixture and its application to a heat-transfer problem, *J. Comput. Phys.* 179 (1) (2002) 201–215.
- [33] M. Sheikholeslami, R. Ellahi, Three dimensional mesoscopic simulation of magnetic field effect on natural convection of nanofluid, *Int. J. Heat Mass Transf.* 89 (2015) 799–808.
- [34] P. Rudolph, Travelling magnetic fields applied to bulk crystal growth from the melt: The step from basic research to industrial scale, *J. Cryst. Growth* 310 (7–9) (2008) 1298–1306.
- [35] A. Kao, Analytic solutions to determine critical magnetic fields for thermoelectric magnetohydrodynamics in alloy solidification, *Metallur. Mater. Trans. A* 46 (9) (2015) 4215–4233.
- [36] S. Yesilyurt, L. Vujisic, S. Motakef, F.R. Szofran, M.P. Volz, A numerical investigation of the effect of thermoelectromagnetic convection (TEMC) on the Bridgman growth of Ge_{1-x}Si_x, *J. Cryst. Growth* 207 (4) (1999) 278–291.
- [37] A. Kao, K. Pericleous, A numerical model coupling thermoelectricity, magnetohydrodynamics and dendritic growth, *J. Algorithms Comput. Technol.* 6 (1) (2012) 173–201.
- [38] P. Lehmann, R. Moreau, D. Camel, R. Bolcato, Modification of interdendritic convection in directional solidification by a uniform magnetic field, *Acta Mater.* 46 (11) (1998) 4067–4079.
- [39] Y.F. Fan, Y. Fautrelle, Z.M. Ren, O. Budenkova, C.J. Li, W.L. Ren, A new method for calculating thermoelectric current during the solidification of alloys, in: 8th International Conference on Electromagnetic Processing of Materials, Oct 2015, Cannes, France. EPM2015 (2015).
- [40] M. Bachmann, V. Avilov, A. Gumenyuk, M. Rethmeier, About the influence of a steady magnetic field on weld pool dynamics in partial penetration high power laser beam welding of thick aluminium parts, *Int. J. Heat Mass Transf.* 60 (2013) 309–321.
- [41] I. Steinbach, F. Pezzolla, B. Nestler, M. Seeßelberg, R. Prieler, G.J. Schmitz, J.L.L. Rezendes, A phase field concept for multiphase systems, *Physica D* 94 (3) (1996) 135–147.
- [42] I. Loginova, G. Amberg, J. Ågren, Phase-field simulations of non-isothermal binary alloy solidification, *Acta Mater.* 49 (4) (2001) 573–581.
- [43] J.A. Warren, W.J. Boettinger, Prediction of dendritic growth and microsegregation patterns in a binary alloy using the phase-field method, *Acta Metall.* 43 (2) (1995) 689–703.
- [44] A. Karma, W.-J. Rappel, Phase-field model of dendritic sidebranching with thermal noise, *Phys. Rev. E* 60 (4) (1999) 3614–3625.
- [45] S.G. Kim, W.T. Kim, T. Suzuki, Phase-field model for binary alloys, *Phys. Rev. E* 60 (6) (1999) 7186–7197.
- [46] I. Steinbach, Pattern formation in constrained dendritic growth with solutal buoyancy, *Acta Mater.* 57 (9) (2009) 2640–2645.
- [47] X. Tong, C. Beckermann, A. Karma, Q. Li, Phase-field simulations of dendritic crystal growth in a forced flow, *Phys. Rev. E* 63 (6) (2001) 061601.
- [48] Y. Sun, C. Beckermann, Diffuse interface modeling of two-phase flows based on averaging: mass and momentum equations, *Physica D* 198 (3–4) (2004) 281–308.
- [49] C. Beckermann, H.J. Diepers, I. Steinbach, A. Karma, X. Tong, Modeling melt convection in phase-field simulations of solidification, *J. Comput. Phys.* 154 (2) (1999) 468–496.
- [50] C.J. Vreeman, F.P. Incropera, The effect of free-floating dendrites and convection on macrosegregation in direct chill cast aluminum alloys Part II: predictions for Al-Cu and Al-Mg alloys, *Int. J. Heat Mass Transf.* 43 (5) (2000) 687–704.

- [51] S. Chen, G.D. Doolen, Lattice Boltzmann method for fluid flows, *Annu. Rev. Fluid Mech.* 30 (1) (1998) 329–364.
- [52] Zhaoli Guo, Chuguang Zheng, Baochang Shi, Discrete lattice effects on the forcing term in the lattice Boltzmann method, *Phys. Rev. E* 65 (4) (2002) 046308.
- [53] X. Li, A. Gagnoud, Z. Ren, Y. Fautrelle, R. Moreau, Investigation of thermoelectric magnetic convection and its effect on solidification structure during directional solidification under a low axial magnetic field, *Acta Mater* 57 (7) (2009) 2180–2197.
- [54] T. Takaki, R. Rojas, S. Sakane, M. Ohno, Y. Shibuta, T. Shimokawabe, T. Aoki, Phase-field-lattice Boltzmann studies for dendritic growth with natural convection, *J Cryst Growth* 474 (2017) 146–153.
- [55] Z.M. Gao, P. Jiang, G.Y. Mi, L.C. Cao, W. Liu, Investigation on the weld bead profile transformation with the keyhole and molten pool dynamic behavior simulation in high power laser welding, *Int. J. Heat Mass Transf.* 116 (2018) 1304–1313.
- [56] A. Farzadi, M. Do-Quang, S. Serajzadeh, A.H. Kokabi, G. Amberg, Phase-field simulation of weld solidification microstructure in an Al–Cu alloy, *Modell. Simul. Mater. Sci. Eng.* 16 (6) (2008) 065005.
- [57] Q. Zhou, Y. Wang, S.-K. Choi, L. Cao, Z. Gao, Robust optimization for reducing welding-induced angular distortion in fiber laser keyhole welding under process parameter uncertainty, *Appl. Therm. Eng.* 129 (2018) 893–906.
- [58] A. Tran, D. Liu, H. Tran, Y. Wang, Quantifying uncertainty in the process-structure relationship for Al–Cu solidification, *Modell. Simul. Mater. Sci. Eng.* 27 (6) (2019) 064005.